THE ASTROPHYSICAL JOURNAL, 545:670–694, 2000 December 20

HUBBLE SPACE TELESCOPE OBSERVATIONS OF VIBRATIONALLY EXCITED MOLECULAR HYDROGEN IN CLUSTER COOLING FLOW NEBULAE[1]

MEGAN DONAHUE, JENNIFER MACK, G. MARK VOIT, AND WILLIAM SPARKS
Space Telescope Science Institute, 3700 San Martin Drive, Baltimore, MD 21218; donahue@stsci.edu, mack@stsci.edu, voit@stsci.edu, sparks@stsci.edu
RICHARD ELSTON
University of Florida, Department of Astronomy, 211 Space Sciences Building, Gainesville, FL 32611-2055; elston@astro.ufl.edu
AND
PHILIP R. MALONEY
University of Colorado, CASA, CB-389, Boulder, CO 80309; maloney@casa.colorado.edu
Received 2000 March 8; accepted 2000 June 30

ABSTRACT

We report the results of *Hubble Space Telescope* near-infrared camera and multiobject spectrometer and Wide Field Planetary Camera 2 imaging of emission-line nebulae in the central galaxies of three clusters of galaxies purported to host massive cooling flows: Perseus (NGC 1275), Abell 2597, and PKS 0745−191. The spectral signature of vibrationally excited molecular hydrogen has been seen in every galaxy searched thus far that is central to a cluster cooling flow with an optical emission-line nebula. With the exquisite spatial resolution available to us with the *Hubble Space Telescope*, we have discovered that the vibrationally excited molecular hydrogen gas extends several kiloparsecs from the centers of Abell 2597 and PKS 0745−191, while the vibrationally excited molecular hydrogen in NGC 1275 appears to be mostly confined to its nucleus, with some extended emission less than 1 kpc from the center. The molecular hydrogen in Abell 2597 and PKS 0745−191 seems to be nearly cospatial with the optical emission-line filaments in those systems. There may be a tiny jet visible in the 1.6 μm image of PKS 0745−191. We also find significant dust absorption features in the 1.6 μm images of all three systems. The dust lanes are not strictly cospatial with the emission-line filaments, but are aligned with and perhaps intermingled with them. The morphology of the emission-line systems suggests that the presence of vibrationally excited molecular hydrogen is not purely an active galactic nucleus–related property of cluster "cooling flow" nebulae, and that the optical and infrared emission-line gas, that is, the ionized and vibrationally excited molecular gas, have similar origins, if not also similar energy sources. The infrared molecular hydrogen lines are much too bright to be generated by gas simply cooling from a cooling flow; furthermore, the gas, because it is dusty, likely did not condense from the hot intracluster medium (ICM). We examine some candidates for heating the nebulae, including X-ray irradiation by the ICM, UV fluorescence by young stars, and shocks. UV heating by young stars provides the most satisfactory explanation for the H_2 emission in A2597; X-ray irradiation is energetically unlikely and strong shocks ($v \gtrsim 40$ km s^{-1}) are ruled out by the high H_2/Hα ratios. If UV heating is the main energy input, a few billion solar masses of molecular gas are present in A2597 and PKS 0745−191. UV irradiation models predict a significant amount of 1.0–2.0 μm emission line from higher excitation H_2 transitions and moderate far-infrared luminosities ($\sim 10^{44}\ h^{-2}$ ergs s^{-1}) for A2597 and PKS 0745−191. Even in the context of UV fluorescence models, the total amount of H_2 gas and star formation inferred from these observations is too small to account for the cooling flow rates and longevities inferred from X-ray observations. We note an interesting new constraint on cooling flow models: the radio sources do not provide a significant amount of shock heating, and therefore they cannot counterbalance the cooling of the X-ray gas in the cores of these clusters.

Subject headings: cooling flows — galaxies: clusters: general — intergalactic medium — ISM: molecules

1. INTRODUCTION

The high density of the hot intracluster medium (ICM) at the centers of many clusters of galaxies implies that this central ICM may cool within a Hubble time. The short cooling time of this gas prompted suggestions that the ICM in these clusters cools and flows toward the center, where it subsequently condenses (see Fabian 1994 and references therein for a review). The central galaxies of clusters suspected to harbor such "cooling flows" frequently display luminous, extended emission-line nebulae (e.g., Heckman et al. 1989), which appear to be ionized and at least partially heated by hot, young stars (Voit & Donahue 1997; Cardiel, Gorgas, & Aragon-Salamanca 1995, 1998; Hansen, Jorgensen, & Norgarrd-Nielsen 1995; Johnstone, Fabian, & Nulsen 1987). The star formation rates inferred from such observations are similar to those in some starburst galaxies (e.g., McNamara 1997). The optical emission-line luminosities from the cooling flow nebulae are strongly correlated (99.94% confidence) with the mass flow rate inferred from the X-ray measurements, albeit with a dispersion spanning up to 2 orders of magnitude (Heckman et al. 1989). The emission-line nebulae are common, appearing in $\sim$40% of X-ray–selected clusters of galaxies (Donahue, Stocke, & Gioia 1992). The emission-line nebulae in clusters seem to avoid clusters with central cooling times longer

[1] Based on observations with the NASA/ESA *Hubble Space Telescope*, obtained at the Space Telescope Science Institute, which is operated by the Association of Universities for Research in Astronomy (AURA), Inc., under NASA contract NAS 5-26555.

than about a Hubble time (Hu 1992). Yet, the optical emission-line gas itself appears to be dusty (Donahue & Voit 1993; Sparks, Ford, & Kinney 1993; Sparks, Macchetto, & Golombek 1989) and thus is not likely to be a direct condensate from the ICM.

The presence of vibrationally excited molecular hydrogen may be as prevalent as optical emission-line nebulae in the central galaxies of cluster cooling flows. All central cluster galaxies with large inferred mass deposition rates and powerful optical emission-line systems observed to date with sufficient sensitivity emit strong molecular hydrogen emission in the 2 μm 1–0 $S(1)$ line (Elston & Maloney 1992, 1994). More recent IR spectroscopic observations of radio galaxies associated with strong cooling flows reveal that these galaxies produce H_2 emission while other radio galaxies do not (Falcke et al. 1998; Jaffe & Bremer 1997). The infrared spectra show H_2 vibrational line ratios characteristic of collisionally excited $\sim$1000–2000 K molecular gas.

Dusty nebular filaments do not appear only in cluster cooling flows. Such structures have also been detected in early-type galaxies in small groups (e.g., Goudfrooij & Trinchieri 1998; Singh et al. 1994) and in interacting gas-rich galaxies (Kenney et al. 1995; Donahue et al. 2000, in preparation). The characteristics in common with cooling flow optical emission-line filaments are the size scales (kiloparsecs) and the prominent forbidden line and recombination emission ([N II], Hα). Some of these sources have had recent interactions. Most of these sources also have hot interstellar medium (ISM) or are embedded in a cluster or group. In none of these objects is the source of the filament energy understood.

This paper is organized as follows: Our targets are described in § 2. In § 3, we describe the observations. Section 4 outlines the data reduction and analysis techniques for both *Hubble Space Telescope* (*HST*) near-infrared camera and multiobject spectrometer (NICMOS) and Wide Field Planetary Camera 2 (WFPC2) data, including construction methods for isophotal profiles, for continuum subtraction from the emission-line flux, and for absolute flux calibration. In § 5, we report and discuss the emission-line fluxes inside the central 2″ of each source. In § 6, we compare the morphology of the molecular gas to the ionized gas, the 1.6 μm dust, and the radio emission. In § 7, we investigate the opacity and reddening of dust at multiple wavelengths. We discuss the implications of our results for the source in § 8 and for the heating mechanism in § 9. We review our conclusions in § 10. We also report our 1.6 μm photometry for the young clusters in NGC 1275 in the Appendix. Luminosities and angular distances are calculated assuming $q_0 = 0.5$ and $H_0 = 100\,h$ km s^{-1} Mpc^{-1}.

2. SAMPLE SELECTION

Three cluster targets, Perseus, Abell 2597, and PKS 0745−191, were chosen for imaging with the *HST* NICMOS camera in order to study the relationship between the vibrationally excited molecular hydrogen, the optical line emitting gas, the dust, and the radio source in the central few arcseconds of X-ray luminous clusters. NGC 1275 is in the center of the Perseus cluster, and PKS 0745−191 is the name of the radio source in the cluster of the same name, but as a convention, we will refer to the central galaxy in Abell 2597 by the name of its host cluster and not by the name of its radio source (PKS 2322−122). All three targets are embedded in cooling flows with significant cooling rates. The nuclei of all three targets were known a priori to emit bright infrared H_2 lines whose observed wavelengths fall within the bandpasses of narrow-band NICMOS filters. Star formation rates inferred from the blue optical excess in all three systems span 10–20 h^{-2} $M_\odot$ yr^{-1} (McNamara 1997). Global target properties are summarized in Table 1.

NGC 1275 is the nearest massive cooling flow, with an inferred cooling rate of $\sim$200 h^{-1} $M_\odot$ yr^{-1} (Edge & Stewart 1991). It is rather atypical for a cooling flow, however, with a luminous active galactic nucleus (AGN) in its center and a foreground, high-velocity system, possibly a colliding galaxy (Hu et al. 1983). Because NGC 1275 is known to be a notoriously complex, albeit bright, cluster cooling flow system, we also observed Abell 2597 and PKS 0745−191, two somewhat more typical cooling flow cluster nebulae that have luminous, unresolved H_2 emission. These two cluster galaxies have among the most luminous 1–0 $S(1)$ nuclear emission observed by Elston & Maloney (1994).

In NGC 1275, there is a large amount of cold molecular gas ($\sim 6 \times 10^9$ $M_\odot$, assuming the debatable standard CO/H_2 conversion) most recently mapped in CO by Bridges & Irwin (1998) and Braine et al. (1995). The CO emission was discovered by Lazareff et al. (1989). In contrast, CO from cold molecular gas has not been detected in PKS 0745−191 (O'Dea et al. 1994b), with an upper limit of 8×10^9 $M_\odot$, again assuming the standard conversion. McNamara & Jaffe (1994) searched six other cooling flow clusters with comparable mass cooling rates for a trace of cold molecular gas (CO) and found nothing with similar limits. Abell 2597 has not been observed in the radio for CO, but notably, it is the only known cluster radio source other than NGC 1275 with H I absorption (O'Dea, Baum, & Gallimore 1994a). Specific comments regarding each source follow here.

NGC 1275.—This is a complex galaxy system with $z = 0.01756$ (Strauss et al. 1992; $1'' = 0.24\ h^{-1}$ kpc, $4\pi d_L^2 = 3.34 \times 10^{53} h^{-2}$ cm^2). It is a Seyfert galaxy (Seyfert 1943), an *IRAS* galaxy (Strauss et al. 1992), a Markarian galaxy, a blazar, the cD galaxy of the Perseus Cluster (Abell 426), a merger system, and a radio source (3C84 or Perseus A). It has a giant nebula of luminous optical emission-line filaments (see Burbidge & Burbidge 1965) extending $\sim$100 kpc from its center. Perseus is the closest example of a cluster of

TABLE 1

TARGET PROPERTIES

Target	Redshift	$\dot{M}$ (h^{-1} $M_\odot$ yr^{-1})	Scale (h^{-1} kpc arcsec^{-1})	kT (keV)	N_H (10^{20} cm^{-2})
NGC 1275	0.0175	250	0.24	6.3	14.5
Abell 2597.....	0.0852	130	1.07	8.5	2.5
PKS 0745−191.....	0.1028	450	1.26	9.1	46.1

TABLE 2

OBSERVING LOG

Target	Camera	Filter	Date	Data Set	Exposure Time (s)
NGC 1275	NICMOS2	F216N	1997 Aug 15	N46001010	1536
		F160W	1997 Aug 15	N46001020	256
		F160W	1998 Mar 16	N3ZB1R010	640
	WFPC2	FR680N	1995 Sep 10	U2S01601T	600
		F702W	1994 Mar 31	U27L1G01T-G04T	560
		F702W	1995 Nov 16	U2PF0402T-405T	4500
		F450W	1995 Nov 16	U2P0407T-40AT	4900
Abell 2597	NICMOS2	F212N	1997 Oct 19	N46003010-3020	12032
			1997 Dec 03	N46004010-4030	
		F160W	1997 Dec 03	N46004ZBQ	384
	WFPC2	F410M	1996 Jul 27	U3CU0101T-104T	2200
		F450W	1995 Jul 05	U2PF0203T-204T	2500
		F702W	1995 Jul 05	U2PF0201T-202T	2100
PKS 0745−191	NICMOS2	F215N	1997 Oct 10	N46002010-2030	7168 (3566)[a]
			1998 Sep 06	N46005010	
		F160W	1997 Oct 10	N46002040	512
	WFPC2	FR680N	1997 Oct 11	U460A201R-204R	3200
		F439W	1997 Oct 11	U460A205R-206R	1000

[a] Effective exposure time for the degraded NICMOS observation in parentheses.

galaxies with a massive cooling flow, with $\dot{M} \sim 250\ h^{-1}\ M_\odot\ \mathrm{yr}^{-1}$ (Peres et al. 1998; Mushotzky et al. 1981; Edge & Stewart 1991). Fischer et al. (1987) first discovered vibrationally excited molecular hydrogen in its nucleus.

A2597.—The central galaxy of Abell 2597 ($z = 0.08520$, Struble & Rood 1987; $4\pi d_L^2 = 8.11 \times 10^{54} h^{-2}$ cm^2, $1'' = 1.07\ h^{-1}$ kpc), also known as PKS 2322−123, is in the center of a massive cooling flow ($\dot{M} \sim 130\ h^{-1}\ M_\odot\ \mathrm{yr}^{-1}$; Crawford et al. 1989). It has a tiny double-sided radio source (Sarazin et al. 1995) and small blue lobes (McNamara & O'Connell 1993), which are relatively unpolarized and thus are thought to be scattered light or synchrotron emission (McNamara et al. 1999). It has an extensive and luminous emission-line nebula (Crawford et al. 1989; Heckman et al. 1989), whose emission lines are inconsistent with being produced by shocks (Voit & Donahue 1997).

PKS 0745−191.—This galaxy ($z = 0.1028$, Hunstead, Murdoch, & Shobbrook 1978; $4\pi d_L^2 = 1.19 \times 10^{55} h^{-2}$ cm^2, $1'' = 1.26\ h^{-1}$ kpc) contains a strong cooling flow, $\sim 450\ h^{-1}\ M_\odot\ \mathrm{yr}^{-1}$ (Allen 2000; Peres et al. 1998; Edge & Stewart 1991; Fabian et al. 1985), a powerful Hα source (Fabian et al. 1985), and like Perseus and A2597, excess blue light in the interior few kiloparsecs (McNamara & O'Connell 1992; Fabian et al. 1985). It is radio loud compared to NGC 1275 ($L_R = 4.5 \times 10^{42} h^{-2}$ ergs s^{-1}), with 5–10 times the radio luminosity of NGC 1275 at 1.4 GHz (Baum & O'Dea 1991).

3. *HST* OBSERVATIONS

High signal-to-noise ratio (S/N) observations of the molecular hydrogen and continuum were acquired with the *HST* NICMOS2 camera, with a pixel size of 0.″075 and a field of view of 19.″2 × 19.″2 (Thompson et al. 1998), using narrowband and broadband filters. For NGC 1275, the narrowband F216N filter allows the observation of the H_2 1–0 $S(1)$ line (rest wavelength 2.12 μm). The other two targets were observed in the 1–0 $S(3)$ line (rest wavelength 1.956 μm), whose nuclear flux is nearly equal to the 1–0 $S(1)$ flux in these systems (Falcke et al. 1998; Elston & Maloney 1994). This line redshifts into the bandpasses of the F215N and F212N NICMOS filters for PKS 0745−191 and A2597, respectively. We obtained broadband F160W images for continuum measurements. The bandpass of the F160W filter ($\sim H$ band) is sufficiently wide and the emission lines sufficiently weak such that the F160W image is of nearly pure continuum light.

To image the optical line emission at a spatial resolution similar to our molecular line maps, we acquired *HST* WFPC2 data (Holtzman et al. 1995), both through our own program and from the Hubble Data Archive. The WF cameras have 0.″0966 pixels and an 80″ × 80″ field of view, while the PC camera has 0.″0455 pixels and a 36″ × 36″ field of view. For NGC 1275, we retrieved archival WFPC2 data taken with the linear ramp filter (LRF) at 6676 Å centered on Hα and [N II] of the low-velocity system. The LRF has a very narrow bandwidth and is "tuned" to the desired central wavelength by appropriate target placement in the field of view. For A2597 we used archival WFPC2 imaging of [O II] λ3727 emission through the F410M filter and of Hα + [N II] emission measured through the F702W filter. The stellar continuum images were taken through the F702W filter for NGC 1275 and the F160W filter for A2597. We observed PKS 0745−191 through the LRF for an Hα image. Blue continuum imaging was carried out using the F439W filter. The total exposure times and observational parameters for each observation are presented in Table 2.

4. *HST* DATA REDUCTION AND CALIBRATION

4.1. *Image Reduction*

HST NICMOS *multiaccum* data may present the observer with significant data reduction challenges, which could not be handled within the current standard *HST* pipeline software called *calnica.* In the following section we describe our infrared data reduction and calibration process, using tasks in the Space Telescope Science Data

Analysis System (STSDAS, Ver. 2.1.1),[2] obtained as a standard package in the publicly available Image Reduction and Analysis Facility (IRAF, Ver. 2.11.3).[3] The solutions we found may prove a useful guide to readers reducing *HST* NICMOS data; therefore, we describe our reductions in moderate detail, citing the software tasks whenever possible. We assume a convention of naming packages in capitals and tasks in italics. We also estimate the magnitude of the systematic uncertainties arising from imperfect data reduction and calibration.

We calibrated the raw NICMOS data and corrected it for various instrument artifacts following methods which were in development by the NICMOS instrument group at the Space Telescope Science Institute (STScI). Images were processed through the first portion of the STSDAS program *calnica*, producing images which are corrected for dark and bias signals and for nonlinearity. Some additive noise, the dark current "pedestal," still exists after this correction and must be removed before the flat-fielding step to prevent imprinting an inverted response pattern on the final image.

To quantify the zeroth-order pedestal in each quadrant, we estimated the mean background signal, excluding sources, which consists of the sky signal plus a constant, quadrant-dependent bias. The initial estimate of the bias level was multiplied by the flat field and subtracted. This process was done independently for each readout frame and quadrant of the total NICMOS exposure. The median residual was then subtracted from each quadrant, and the root mean square variation of the resulting background was measured. This process was repeated for a range of initial guesses to deduce the value which minimized the root mean square variation of the background and, thus, of the influence of the large-scale flat-field pattern. It was necessary to be very careful when subtracting the background from these images, because the outer isophotes of the galaxy also contribute to the large-scale background signal. When the source fills the majority of the frame, separating the bias, sky background, and galaxy light is more difficult. We obtained our best results when we subtracted the pedestal after removing the target galaxy by fitting its surface brightness profile and subtracting the profile from the data.

A residual, noiseless spatial variation, called "shading," in the bias after dark subtraction remained in only a few of the narrowband A2597 images, resulting in a position-dependent, low-level background. The bias changes slowly across the field of view, and again, if not removed, it results in an imprint of the flat-field pattern left in the data. The "shading" pattern results because the reference dark image does not precisely reproduce the temperature-dependent dark current if the temperature of the detector varied or was different from that of the reference dark image.

To correct for this small effect, we modeled the background outside the central $7\farcs5 \times 7\farcs5$ box by median filtering the image with a boxcar size of 13×13 pixels and subtracted the resulting median background from the pixels outside the central box region. This procedure, mostly cosmetic, brings out the contrast of the central structures without changing the value of the mean background. The effect of not fully correcting for this additional additive background in the central $7\farcs5$ adds an additional systematic uncertainty in the absolute H_2 emission-line fluxes for A2597 of $\sim 5\%$ after flat-fielding. (Systematic uncertainties in the H_2 fluxes arising from calibration are $\lesssim 5\%$ without this effect.)

After we estimated and subtracted the effective dark current, the standard *calnica* process flat-fielded the data, corrected for cosmic rays, and converted the units to counts (or DN, digital number) s^{-1}.

The final challenge was to correct for cosmic ray persistence. NICMOS images taken very soon after *HST* passes through the South Atlantic Anomaly radiation belt are affected significantly by cosmic ray persistence and thus are degraded by noise. The decaying afterglow from energetic cosmic rays persist from one read of the detector to the next, causing the signal from a single cosmic ray event to persist from one read to the next. Two-thirds of our narrowband images of PKS 0745 were significantly impacted by persistence. We took significant amounts of off-source data for the narrowband observations, originally to enable the removal of any significant thermal component at 2 μm. To remove persistent cosmic ray contamination, we modeled the charge decay rate by scaling the off-source images taken later in time and subtracting the scaled image from the initial on-source image. This procedure was iterated until we found a constant value which minimized the root mean square variation of the background. For our affected images, this procedure improved the overall S/N by about 30%. Finally, we aligned these processed images and combined them into a single weighted average image.

WFPC2 data are much easier to calibrate, and the standard STSDAS pipeline procedure *calwp2*, with the standard updated reference files, was used to process our data. The LRF images were flat-fielded with the narrowband filter flat of the nearest available wavelength (filter F673N; WFPC2 Instrument Science Report 96-06).[4] Images were combined and cosmic rays removed using the STSDAS task *crrej*.

4.2. *Isophotal Fitting and Continuum Subtraction*

Isophotal fitting of the NICMOS data was performed for the inner $7''$ radial region of each galaxy using the STSDAS task *ellipse*. All parameters (ellipticity, position angle, and center position) were left free to fit the *H*-band (F160W) continuum. A continuum model was created using the best-fit parameters. A similar ellipsoidal fit was made to the narrowband data, but with the ellipticity, position angle, and centroid fixed to those parameters modeling the continuum data. The difference between the narrowband data and the continuum model, appropriately scaled, provides an estimate of the total amount and extent of the residual H_2 emission. The relative scale factor (Table 3, Isophotal counts ratio) was determined by matching the galaxies' isophotal profiles, assuming that at large radii ($\sim 4''$–$7''$) the smooth flux is purely from the galaxy's stellar component. Since the isophotes should be the same shape at large radii, this last assumption provides a means of assessing the quality of our background subtraction. The background in the narrowband images consists of three independent quantities: the bias offset, the sky flux, and the continuum. If the background is oversubtracted, the galaxy's isophotal profile takes a characteristic sharp turn downward at large radii. By minimizing this "edge," we were able to fine-tune our background subtraction for images with low S/N and thus

[2] http://ra.stsci.edu/STSDAS.html.

[3] http://iraf.noao.edu/iraf-homepage.html.

[4] http://www.stsci.edu/instruments/wfpc2/Wfpc2_isr/wfpc2_isr9606.html.

TABLE 3

MOLECULAR LINE AND OPTICAL LINE PARAMETERS

Parameter	NGC 1275	A2597		PKS 0745−191
z	0.01756	0.08520		0.1028
H_2 line transition	1–0 $S(1)$	1–0 $S(3)$		1–0 $S(3)$
Observed wavelength (μm)	2.157	2.123		2.157
Continuum filter	F160W	F160W		F160W
Line filter	F216N	F212N		F215N
Line filter FWHM (Å)	181.6	206.8		189.1
γ_c (eq. 1)	1.09	1.00		1.25
Nuclear line FWHM (Å)	50[a]	50[a]		55[b]
Isophotal counts ratio	0.056	0.060		0.055
Predicted throughput ratio	0.056	0.056		0.052
Optical emission line	Hα	Hα	[O II]	Hα
Observed wavelength (Å)	6678	7122	4045	7237
Hα/Hα+[N II]	0.44[c]	0.41[d]		0.38[e]
Continuum filter	F702W	F160W	F450W	F439W
Line filter	LRF	F702W	F410M	LRF
Line filter FWHM (Å)	77.7	1381.6	219.4	84.1
γ_c (eq. 1)	1.00	1.08	1.09	1.00
Nuclear line FWHM (Å)	18[c]	15[d]	13[d]	12[e]
Isophotal counts ratio	0.041	0.087	0.110	0.387
Predicted throughput ratio	0.043	0.693*	0.112	0.169*

NOTE.—The asterisks (*) denote the two cases where continuum and emission filters were centered on significantly different wavelengths and thus the flat spectrum assumption breaks down.

[a] Elston & Maloney 1994.

[b] Falcke et al. 1998.

[c] Palomar Double Spectrograph spectrum (M. Donahue 1993, unpublished).

[d] Voit & Donahue 1995.

[e] Donahue & Stocke 1994.

improve our ability to subtract the continuum from the narrowband images.

To test the reliability of this technique of scaling the continuum images, we used the synthetic photometry package SYNPHOT (available in STSDAS within IRAF) to derive the relative flux scale an alternate way: by calculating the expected change in continuum throughput from filter to filter. Using the task *bandpar*, we were able to estimate the ratio of throughput efficiency for each filter pair for a flat-spectrum (in F_λ) source, where the efficiency is defined as the integral over wavelength of the total filter throughput. These values are given in Table 3 (Predicted throughput ratio) and show strong agreement with the isophotal predictions, except in the two cases (flagged with asterisks) where the optical continuum filter is of a significantly different wavelength than the emission. In order to desensitize our final results to assumptions regarding the underlying continuum spectra, we based our continuum subtraction on the isophotal profiles.

Because the effects of dust obscuration are much less significant at 1.6 μm than at shorter wavelengths, we removed the continuum from the WFPC2 emission-line images by fixing the isophotal parameters to match those parameters obtained from the 1.6 μm data. For NGC 1275, the bandpass of the companion broadband filter also contains the wavelength of the optical emission line of interest, but the filter is wide enough that contamination is only a few percent, and thus the net profile and line fluxes should not be significantly affected.

We present the isophotal profiles for each galaxy in Figure 1, with magnitudes per unit sky area provided in arbitrary units. All of the NICMOS narrowband images clearly show H_2 line emission within the central arcsecond of each cooling flow, and all three galaxies show additional extended emission, out to a radius of about 2″–3″. The optical continuum for all of the galaxies of course extends beyond the central 8″. We present a morphological comparison of both the ionized and the vibrationally excited molecular gas in § 6.

4.3. *Absolute Flux Calibration*

We describe here our process for estimating absolute fluxes for the emission-line images. Once the residual emission images were created, we converted their count rates to units of absolute flux using the SYNPHOT package. For continuum observations of broadband sources, the standard *HST* flux calibration provides the correct absolute flux conversion with the overall photometric accuracy better than 5% for the NICMOS data, 2% for the WFPC2 wide- and medium-band filters, and 3% for the WFPC2 linear ramp filters. A standard method to estimate the flux of a single emission line in ergs s^{-1} cm^{-2} is to assume that the spectrum of the continuum emission is flat (in F_λ) and then to correct for the contribution of the emission line. The following approximation is usually made for *HST* imaging:

$$F_{\rm line} = {\rm CR} * \gamma_c * 1.054 * \Delta\lambda * {\rm PHOTFLAM}\ , \quad (1)$$

where CR is the flux in DN s^{-1}, $\Delta\lambda$ is the Gaussian width of the filter bandpass, PHOTFLAM is the flux conversion factor for the standard *HST* flux calibration from the *HST* data header (in units of ergs cm^{-2} $Å^{-1}$ DN^{-1}), and γ_c is a correction factor to account for the position and width of

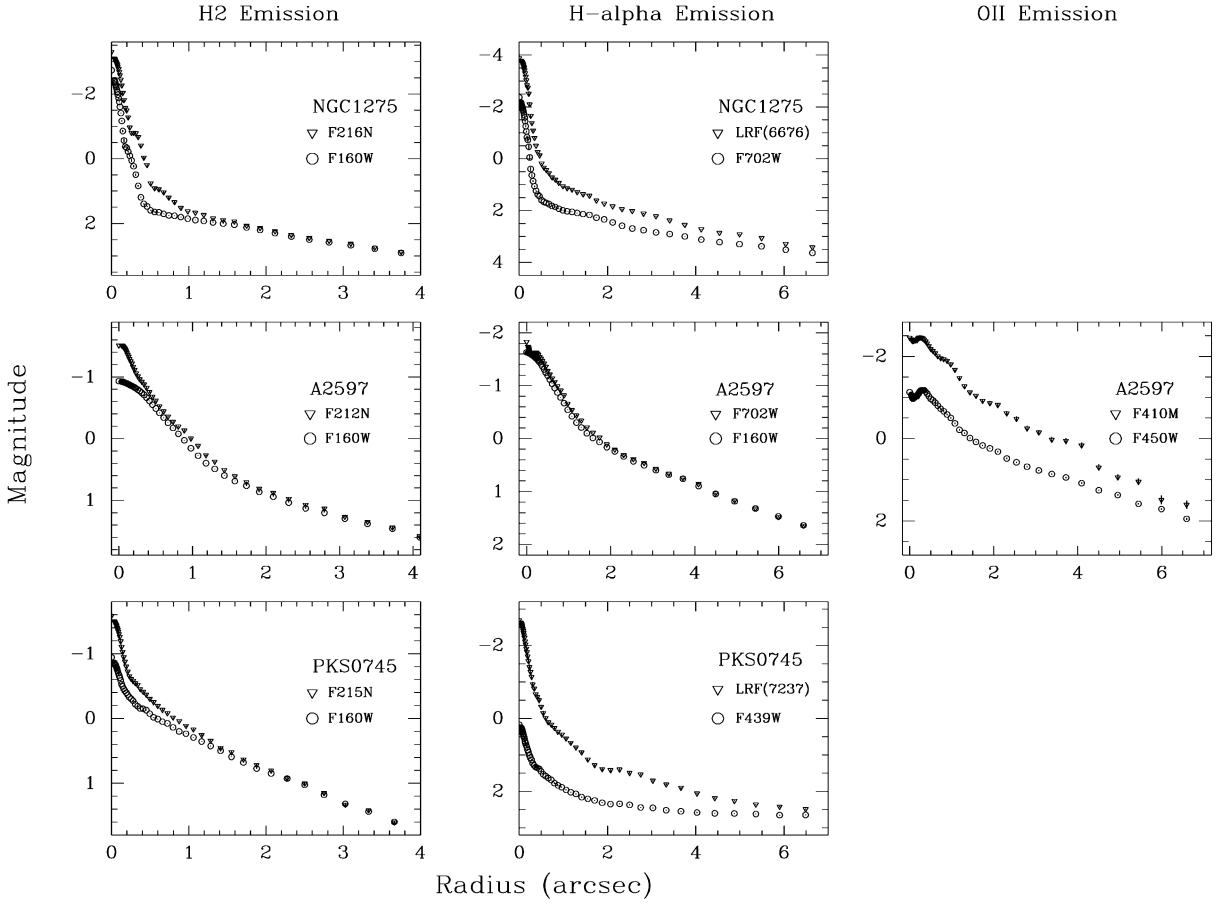

FIG. 1.—Isophotal profiles of each source in the wide and narrow bandpasses

the emission line in the filter bandpass ($\gamma_c = 1$ when the line falls at the filter center; *HST* Data Handbook Ver. 3.1, § 18.2.5).[5] To estimate γ_c, we used SYNPHOT to model the instrumental throughput for each filter, we assumed the emission lines to be Gaussian-shaped, and we used the H_2 line widths (FWHM) given in Table 3. A DN is a "digital number," or a count, and is equal to the number of electrons read out from a pixel multiplied by the detector gain.

We tested the robustness of the standard method by modeling a flat spectrum plus a single emission line first, then calculating the appropriate flux conversion. (See the WFPC2 Instrument Science Report 96-06 describing these methods for the photometric calibration of the LRFs.)[4] SYNPHOT convolves an emission-line model of a given flux in ergs s^{-1} cm^{-2} and the appropriate Gaussian line width with the known throughput of the telescope in each relevant observing mode. SYNPHOT then returns the flux (in DN s^{-1}) that would be expected for each observation. Both methods discussed give similar results for a single Gaussian line, agreeing to within 5% or less.

However, each Hα observation also included [N II] in its filter bandpass. The ratio of Hα to the Hα + [N II] emission for the central 2″ of each cluster is reported in Table 3, from ground-based spectroscopy. To determine the net flux of Hα emission, we had to estimate the contribution from [N II] in each filter. For A2597, the F702W filter is sufficiently wide that the observed spectroscopic line ratios could be employed to correct the total measured flux for [N II] contamination. The linear ramp filters used to observe NGC 1275 and PKS 0745−191, on the other hand, are quite narrow, and transmission falls off rapidly away from the filter center, and thus requires a more sophisticated approach. To provide the most accurate estimate of pure Hα, we determined the flux calibration for the specific case of the Hα + [N II] line complex by convolving the appropriate filter and telescope response functions with three Gaussian lines centered at 6548 Å, 6563 Å, and 6583 Å, having the appropriate relative flux ratios, line widths, and redshifts measured from nuclear spectra for each of the three galaxies (Table 3). This correction increases the nominal flux conversion factor by 10% for NGC 1275 and PKS 0745−191. We then corrected the total measured flux using the spectroscopic [N II]/Hα line ratios (Table 3).

The sensitivity of our flux calibrations to uncertainties in line widths and to the relative contributions of [N II] and Hα emission was also tested. The widths of the emission lines could be smaller for off-nuclear regions (H II regions, for example) than they are in the cores of the galaxies. The flux conversion factor for H_2 emission decreases by 8%, 1%, and 20% for NGC 1275, A2597, and PKS 0745−191, respectively, if a FWHM of 5 Å rather than 50 Å is assumed. For the Hα line, decreasing the assumed FWHM by a factor of ∼10 to 2 Å results in a 2% flux decrease for NGC 1275 and in no change for the other two targets. The [N II]/Hα ratio assumed in our calculations is an average value from ground-based long-slit observations and could vary spatially. Varying the assumed [N II]/Hα ratio between 0.5 and

[5] http://www.stsci.edu/documents/data-handbook.html.

1.5 changes the total (Hα + [N II]) measured flux very little, altering the total flux of NGC 1275 and A2597 by 4% and PKS 0745−191 by 1%. However, the inferred Hα flux could vary by a factor of 2.0 between these two extremes, to be between 60% and 33% of the total measured flux. Therefore, off-nuclear pure Hα estimates are only good to about a factor of 2. The absolute infrared H_2 flux calibration is good to at least 25% off-nucleus, where hot dust from the central torus is unlikely to contaminate our measurements, and to approximately a factor of 2 on-nucleus, lacking an estimate for the hot dust contribution. The uncertainties quoted in the following tables do not include these systematic calibration uncertainties, but we take them into account when we compare these data to model predictions.

5. APERTURE PHOTOMETRY

The derived isophotal profiles indicate excess 2 μm emission in the central few arcseconds of each galaxy. We know from previous spectroscopy that each of the galactic nuclei produces H_2 emission and that the continuum emission between 1.5 and 2.0 μm is fairly flat. So our absolute photometry in the *H* band and 2 μm narrowband filters should allow us to subtract the continuum in the nuclei fairly accurately. We checked this by comparing the continuum scale factor derived from absolute photometry (§ 4.2) to that derived from matching the galaxy surface brightness profiles at the edges of the NICMOS field of view. Nevertheless, as mentioned in § 4.3, our estimates of H_2 emission in the nuclei, where the AGN and hot dust from the central torus dominate, cannot be precise because of the limitations on our technique.

The net H_2 surface brightness was measured from each residual image within concentric annular apertures centered on the galaxy. In Figure 2, the net surface brightness of the H_2 emission, the Hα + [N II] ("optical") emission, and the molecular-to-optical flux ratio for the inner 4″ of each galaxy is plotted. Spurious behavior of the flux ratios at radii less than 0.″4 is an effect of the NICMOS point-spread function (PSF) and its Airy ring. The total H_2 fluxes, measured within a radius of 2″, are presented in Table 4. The fluxes in these tables have been corrected for Galactic reddening and absorption but not for intrinsic reddening or absorption.

NGC 1275.—For NGC 1275, the molecular emission is concentrated in the nucleus of the galaxy. To determine its extent, we compared the radial profile of a typical star with the radial profile of the NGC 1275 nucleus in the narrowband image. The measured characteristic radius of the NGC 1275 nucleus was only slightly larger than that of the PSF star, implying an intrinsic radial scale of less than 0.″09 (∼1–1.2 pixels) for the residual emission, corresponding to a physical scale of $\lesssim 22\,h^{-1}$ pc. The H_2 emission-line flux of the central source within a 2″ radius aperture was measured to be $(9.84 \pm 0.34) \times 10^{-14}$ ergs s^{-1} cm^{-2}, corresponding to an H_2 line luminosity of 3.3×10^{40} ergs s$^{-1}h^{-2}$. Faint extended emission is detected up to 2″ off-nucleus.

The AGN in NGC 1275 is known to be variable, so comparison of photometry from different epochs may not be relevant, but we report earlier flux estimates here. Inoue et al. (1996) measured the total flux of 2 μm molecular emission in NGC 1275 for a 2″ × 2″ region in the center and derived a value of $(2.5 \pm 0.1) \times 10^{-14}$ ergs s^{-1} cm^{-2}. Using a similar area aperture ($r = 1.''13$), we measured $(9.4 \pm 0.3) \times 10^{-14}$ ergs s^{-1} cm^{-2}. The ground-based Inoue et al. (1996) observations, done with a 2″ × 30″ slit, may not have been well centered on the central source and

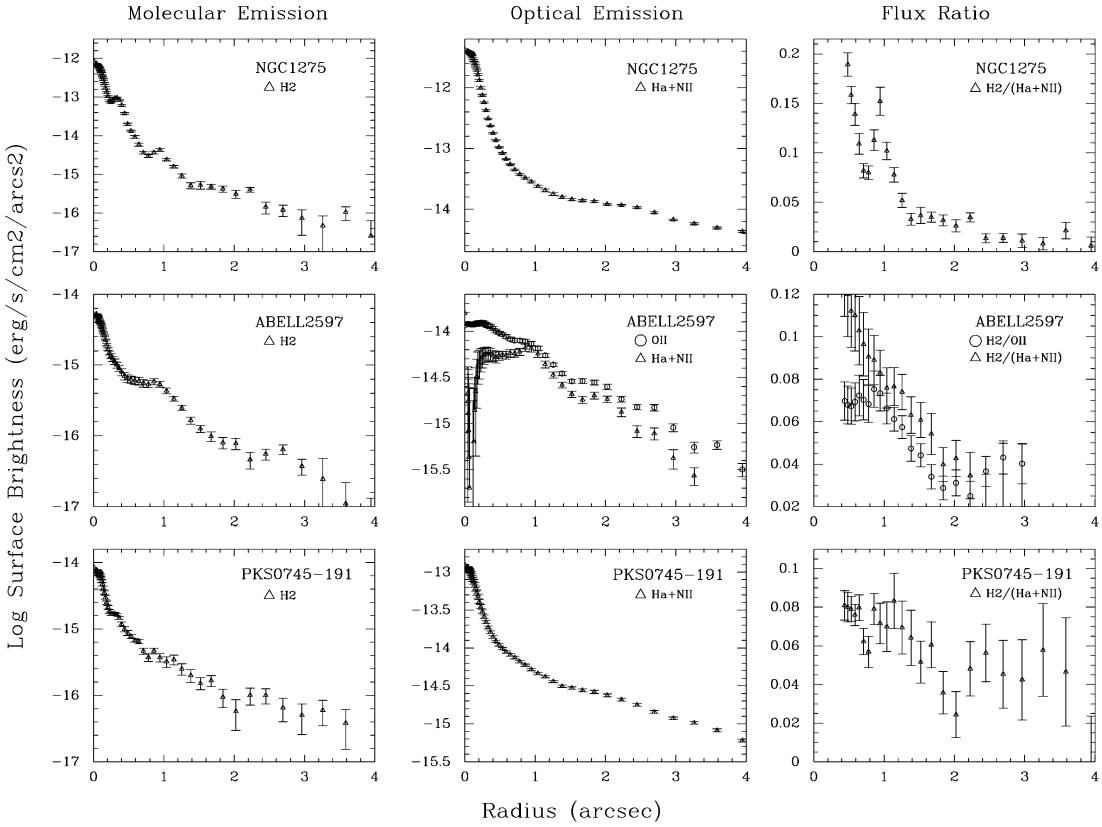

FIG. 2.—Continuum-subtracted emission-line surface brightness and surface brightness ratios as a function of radius

TABLE 4

APERTURE ($r = 2''$) PHOTOMETRY SUMMARY

Parameter	NGC 1275	A2597	PKS 0745−191
Flux H_2(DN s^{-1})	176.6 ± 6.02	7.09 ± 1.23	6.73 ± 1.21
Flux Hα+[N II] (DN s^{-1})	170.0 ± 6.11	10.88 ± 1.53	10.22 ± 1.22
Flux [O II] (DN s^{-1})		2.93 ± 0.82	
Flux H_2 ergs s^{-1} cm^{-2}	(9.84 ± 0.34) x 10^{-14}	(3.71 ± 0.64) x 10^{-15}	(4.63 ± 0.83) x 10^{-15}
Flux Hα+[N II] ergs s^{-1} cm^{-2}	(7.64 ± 0.27) x 10^{-13}	(4.15 ± 0.58) x 10^{-14}	(6.44 ± 0.77) x 10^{-14}
Flux [O II] ergs s^{-1} cm^{-2}		(5.87 ± 1.66) x 10^{-14}	
Luminosity H_2 h^{-2} ergs s^{-1}	(3.3 ± 0.1) × 10^{40}	(3.0 ± 0.5) × 10^{40}	(5.5 ± 1.0) × 10^{40}
Luminosity Hα+[N II] h^{-2} ergs s^{-1}	(2.6 ± 0.1) × 10^{41}	(3.4 ± 0.5) × 10^{41}	(7.7 ± 0.7) × 10^{41}
Luminosity [O II] h^{-2} ergs s^{-1}		(4.8 ± 1.3) × 10^{41}	

the conditions were not perfectly photometric. Inoue et al. (1996) noted possible variable seeing and/or tracking problems with the standard star. Both problems would also affect flux estimates from a slit observation. They also note a flux deficit with respect to earlier H_2 observations by Kawara & Taniguchi (1993) (3.8×10^{-14} ergs s^{-1} cm^{-2} in the central $2''.5 \times 3''.0$). Krabbe et al. (2000) report ground-based fluxes of 4.1×10^{-14} ergs s^{-1} cm^{-2} in the central $3''$. This discrepancy suggests that our estimate could be contaminated by hot dust continuum from the AGN, contributing almost the same flux as the H_2 line to the narrowband excess on the nucleus. Our off-nuclear surface brightness estimates are consistent with Krabbe et al. (see next section).

In contrast to the compact vibrationally excited molecular hydrogen emission, the Hα line emission completely pervades the PC field of view. Optical line emission through the WFPC2 LRF is detected to the edge of the field; the precise surface brightness of the extended emission is difficult to quantify because the central wavelength of the LRF and the redshift of the emission-line gas varies across the field. The emission-line widths are relatively broad, and the bandpass of the LRF at any position is relatively narrow; thus, varying fractions of the [N II]+Hα line complex are imaged, depending on the position in the field. The location of the nucleus of NGC 1275 is such that it is centered on the observed wavelength of Hα. The Hα+[N II] emission in an aperture of radius $2''$ is $(7.6 \pm 0.3) \times 10^{-13}$ ergs s^{-1} cm^{-2}, and thus $F_{H\alpha}$ is $(3.3 \pm 0.2) \times 10^{-13}$ ergs s^{-1} cm^{-2}. The ratio of Hα to 1–0 $S(1)$ H_2 line emission in the nucleus of NGC 1275 is 3:7 ($r < 2''$, corrected for [N II] contribution and for a contribution of warm dust continuum ranging from 0% to 50% of the estimated 2 μm excess in the nucleus; the ratio is uncorrected for internal absorption).

A2597.—In A2597, the narrowband infrared images reveal a complex, multicomponent structure of vibrationally excited molecular hydrogen extending over $2''$ north and east of the nucleus. The location of the nucleus is revealed in the 1.6 μm image behind the thick dust absorption feature seen in the optical images. The complex structure of the emission gas is apparent in the differential flux profiles of A2597. The radial surface brightness profile of [O II] λ3727 decreases sharply at a radius of $0''.3$, where a thick dust lane obscures the galaxy's core. Within an aperture radius of $2''$, we derive a total H_2 flux of $(3.7 \pm 0.6) \times 10^{-15}$ ergs s^{-1} cm^{-2}, corresponding to an emission-line luminosity of $3.0 \times 10^{40} h^{-2}$ ergs s^{-1}.

We subtracted a scaled H-band image from the F702W image to reveal the emission-line system in Hα+[N II]. The Hα image shows the same filamentary structure as does the [O II] image (Koekemoer et al. 1999), with an Hα+[N II] flux of $(4.15 \pm 0.58) \times 10^{-14}$ ergs s^{-1} cm^{-2} within $2''$ or an Hα flux of $(1.6 \pm 0.2) \times 10^{-14}$ ergs s^{-1} cm^{-2} and an [O II] flux of $(5.9 \pm 1.7) \times 10^{-14}$ ergs s^{-1} cm^{-2} inside $2''$, corresponding to optical emission-line luminosities of $1.3 \times 10^{41} h^{-2}$ ergs s^{-1} and $4.8 \times 10^{41} h^{-2}$ ergs s^{-1}, respectively. The ratio of Hα to 1–0 $S(3)$ H_2 emission in the central $2''$ is formally 4.3 ± 0.9, corrected for [N II] but uncorrected for internal absorption.

PKS 0745−191.—Emission from the H_2 gas within the central galaxy of PKS 0745−191 is concentrated in the core of the galaxy and in a bright clump just off the nucleus. The total H_2 flux within a radius of $2''$ (or 2.52 h^{-1} kpc) is $(4.6 \pm 0.8) \times 10^{-15}$ ergs s^{-1} cm^{-2}, corresponding to a 1–0 $S(3)$ line luminosity of $5.5 \times 10^{40} h^{-2}$ ergs s^{-1}. The total net Hα+[N II] emission-line flux from the same region is $(4.6 \pm 0.8) \times 10^{-13}$ ergs s^{-1} cm^{-2}, or Hα alone of $(2.6 \pm 0.3) \times 10^{-13}$ ergs s^{-1} cm^{-2}. The ratio of Hα to 1–0 $S(3)$ H_2 emission in the central $2''$ is 5.7 ± 1.2, corrected for [N II] but uncorrected for internal absorption.

6. EMISSION-LINE MAPS

The morphology of the emission from the ionized gas, the vibrationally excited molecular gas, and the dust absorption were compared for each source. In Figures 3, 4, and 5, we present side-by-side gray-scale comparisons of the molecular hydrogen emission and optical line emission along with the red starlight, the dust, and the radio emission for the central regions of each galaxy. We mapped the obscuration due to dust at 1.6 μm by dividing each image by its isophotal model and binning the residual. For comparison with radio structures on the same angular scales, we sought radio maps from the literature with angular resolution similar to that of *HST*. Maps obtained at 666 MHz for NGC 1275 (Pedlar et al. 1990), at 8.44 GHz for A2597 (Sarazin et al. 1995), and at 2 cm and 6 cm for PKS 0745 (Baum & O'Dea 1991) are contoured over *HST* gray-scale images. All of the images of a given target are plotted at the same angular scale and orientation.

The emission-line maps show what the aperture photometry and the radial surface brightness plots only suggested: most of the molecular hydrogen emission from NGC 1275 is confined to the nucleus, except for faint wisps to the southwest and northeast, while the emission from A2597 and PKS 0745−191 is clearly extended. The maps reveal that this extended emission is filamentary and traces very similar structures, as does the optical line emission. We

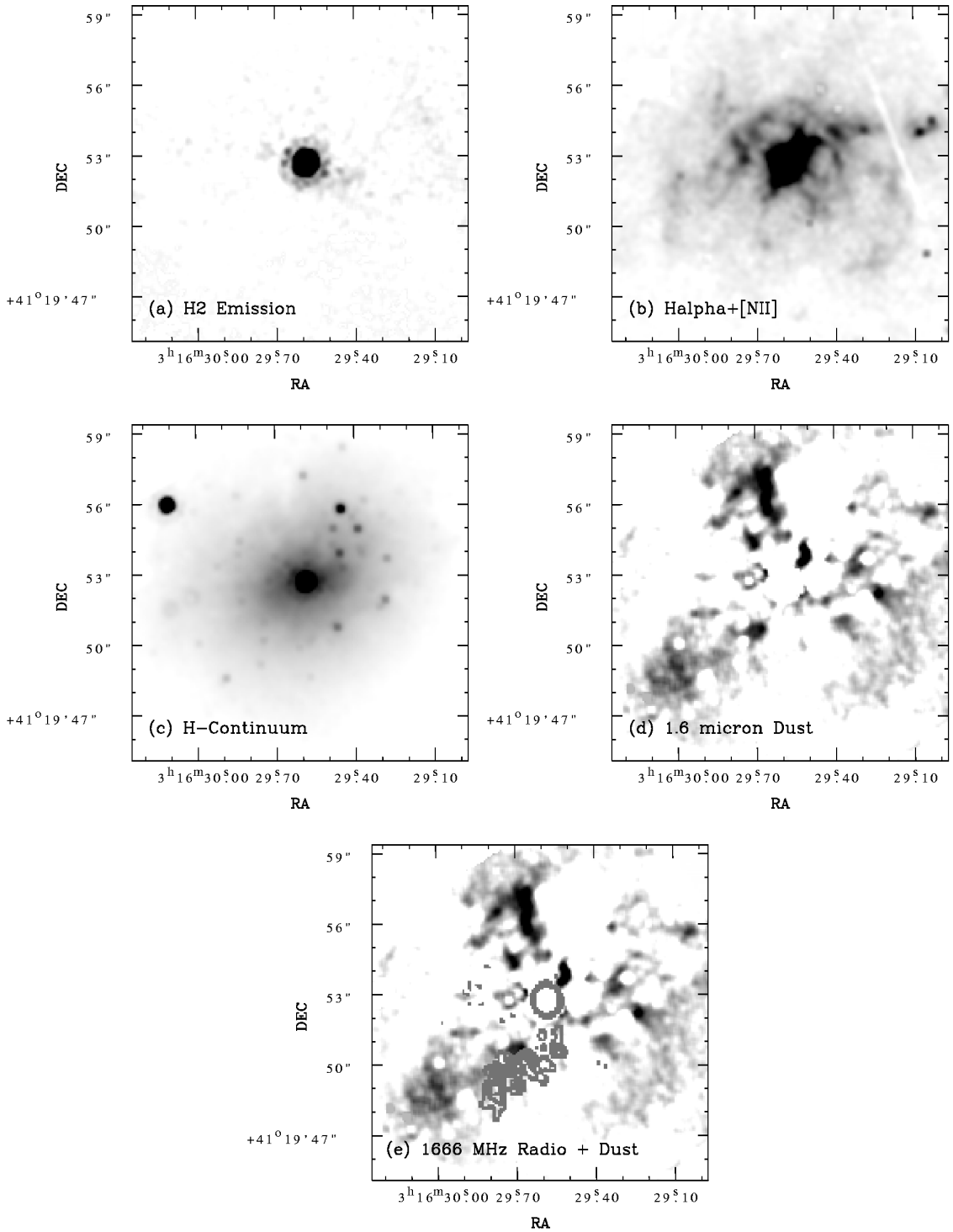

FIG. 3.—Multifrequency images of NGC 1275. (*a*) H_2 emission; (*b*) Hα+[N II] emission; (*c*) *H*-band continuum; (*d*) 1.6 μm dust (darker regions are dustier); (*e*) 151 MHz radio emission contours overlaid on a gray-scale Hα+[N II].

report a possible jet feature in PKS 0745−191. We now discuss each source in turn.

NGC 1275.—While extended, filamentary Hα emission fills the central region of NGC 1275 (Fig. 3*b*), we detected H_2 emission mostly in the nucleus of the galaxy (Fig. 3*a*). The H_2 residual image exhibits the pattern of the NICMOS PSF and its first Airy ring, with no structure detected at larger radii. There is a faint trail of emission off to the southwest of the nucleus and a small blob east of the nucleus. These features were also seen in ground-based images by Krabbe et al. (2000). We measured similar surface brightnesses. In a $1'' \times 1''$ box, the mean surface brightness of the trail feature is $(1.5 \pm 0.8) \times 10^{-15}$ ergs s^{-1} cm^{-2} arcsec^{-2}, consistent with Krabbe's estimated 2×10^{-15} ergs s^{-1}cm^{-2}arcsec^{-2} for the same feature.

The surface brightness limit for undetected features was computed by masking the obvious point sources in the residual H_2 image and median filtering the residual within a

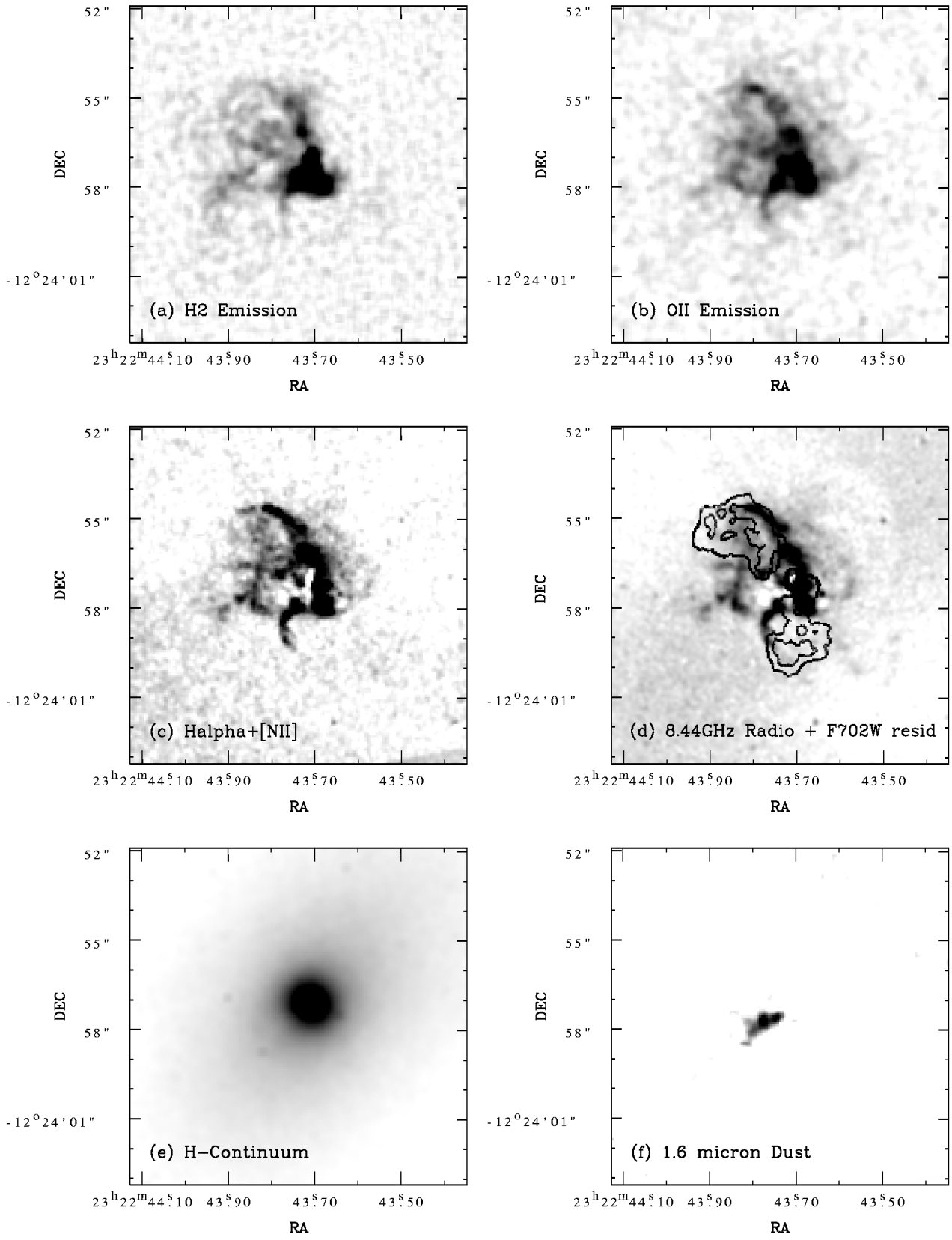

FIG. 4.—Multifrequency images of A2597. (*a*) H_2 emission; (*b*) [O II] emission; (*c*) Hα + [N II] emission; (*d*) 8.44 GHz radio emission (Sarazin et al. 1995) contours overlaid on a gray-scale image of the F702W isophotal residual image, emphasizing the blue lobes (seen here in white negative) to the northeast and southwest of the radio source; (*e*) *H*-band continuum; (*f*) 1.6 μm dust (darker regions are dustier).

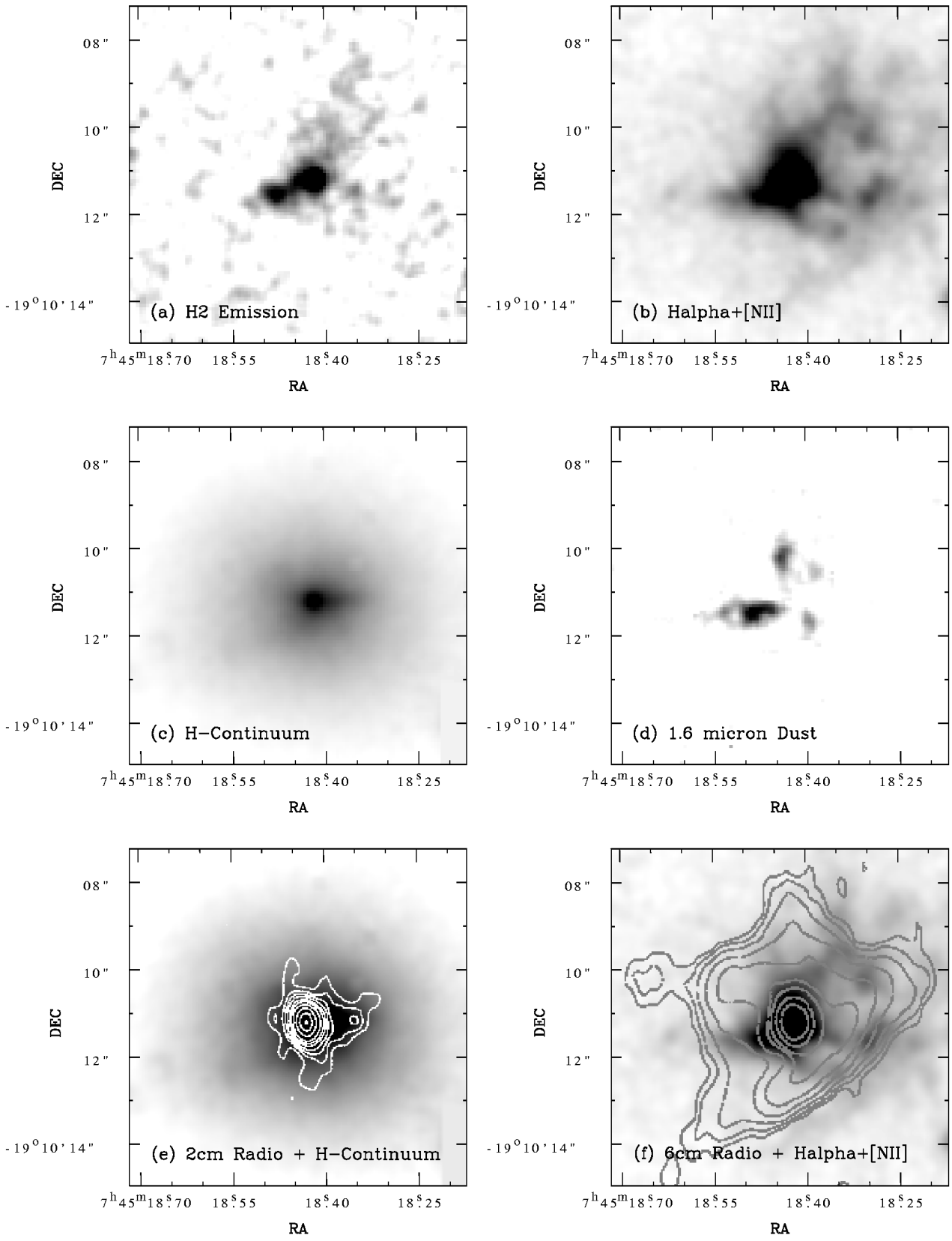

FIG. 5.—Multifrequency images of PKS 0745−191. (*a*) H_2 emission; (*b*) Hα+[N II] emission; (*c*) *H*-band continuum; (*d*) 1.6 μm dust; (*e*) 2 cm radio contours from Baum & O'Dea (1991) overlaid on 1.6 μm image, emphasizing the jet feature; (*f*) 6 cm radio emission contours (Baum & O'Dea 1991) overlaid on Hα+[N II] gray-scale image.

smoothing kernel of a 13 × 13 pixel box. The mean net sky value was 0.00 ± 0.005 DN s^{-1} $pixel^{-1}$, corresponding to a 2 σ surface brightness threshold of 5×10^{-16} ergs $s^{-1}cm^{-2}arcsec^{-2}$.

Hα+[N II] emission-line surface brightness in the same region was as intense as 2×10^{-14} ergs $s^{-1}cm^{-2}arcsec^{-2}$ in a filament 3″ west of the nucleus and 5×10^{-14} ergs $s^{-1}cm^{-2}arcsec^{-2}$ in a bright feature extending 1″ west-northwest of the nucleus. The total amount of Hα contributing to the emission-line flux is approximately half of the surface brightness in Hα+[N II]. Therefore, in these bright optical filaments and features, the Hα/1–0 $S(1)$ H_2 line ratio is greater than $\sim$20 and $\sim$40, respectively. These line-ratio limits are consistent with line ratios expected from shocked gas in which the molecules have been largely dissociated ($v_s \gtrsim 40$ km s^{-1}).

The 1.6 μm image (Fig. 3*c*) shows a smooth stellar continuum and some dust lanes, along with some of the stellar clusters that were reported in WFPC2 optical observations by Holtzman et al. (1992). We report the IR photometry of the brightest of these clusters in the Appendix. The exposure time for our Guest Observer (GO) image was only 256 s, but this image was improved by co-adding an archival snapshot image of 640 s. The residual 1.6 μm continuum image (Fig. 3*d*) is displayed such that the regions with dust (negative residuals) are gray or black and the lighter areas are regions with less or no detectable absorption. The absorption map reveals that the central region is embedded in filamentary dust features which wind inward as close as 0.″5 from the center. The features do not identically track the morphology of the Hα emission-line filaments. Some regions of strong dust absorption also seem to have powerful Hα emission, such as the region just northwest of the nucleus, but for the most part the dust features are at best tangled with the ionized gas filaments. The 666 MHz radio contours (Pedlar et al. 1990) show the AGN point source and a feature extending southeast parallel to a dust feature.

A2597.—The residual H_2 emission map (Fig. 4*a*) shows very distinct filamentary structure extending from the nucleus of the galaxy. This extended, filamentary network traces the complex structure found in both the Hα and the [O II] emission maps (Figs. 4*b* and 4*c*) derived from archival WFPC2 observations. Several bright filamentary arms extend outward from the nucleus and arc counterclockwise like tiny spiral arms or tidal tails. The brightest knot of H_2 emission is in the core of the galaxy. This has no direct counterpart in either of the optical emission images, likely because of substantial dust obscuration of the center of the galaxy. The optical emission profiles for Abell 2597 are rather flat inside 1″ and certainly not as peaked as the molecular line surface brightness, which may imply that dust may be absorbing the optical line emission at least in the central square arcsecond.

The 1.6 μm stellar continuum image (Fig. 4*e*), on the other hand, is quite smooth, with some very faint features which are hot pixels not completely subtracted by processing. The residual 1.6 μm absorption image shows little dust absorption (Fig. 4*f*), except for one thick lane extending southeast from the nucleus. This dust lane is offset to the north of the nearby emission arm but is directly adjacent to it. The edges of the radio lobes trace the gas emission and the dust lane extremely well, with the leading edge of each radio lobe aligning precisely with a bright filamentary arm (Fig. 4*d*). These small-scale radio lobes are also correlated with the lobes of blue light, seen best in the F702W isophotal residual image (Koekemoer et al. 1999). The radio source appears to be interacting with the ambient gas and possibly also the dust. This interaction with the ICM may have induced star formation and would thus explain the presence of the blue lobes (McNamara et al. 1993; Koekemoer et al. 1999). In Figure 6, the brightest emission clumps which were found in both the optical and infrared emission-line images are labeled, and we present the flux ratios of these two components in Table 5.

The core of the *ROSAT* HRI image of A2597 shows some east-west elongation at the smallest scales resolvable by the HRI ($\sim$4″; Sarazin et al. 1995; Pierre & Starck 1998), which may indicate that the ICM of A2597 and the ISM of PKS 2322−12 (the central radio source of A2597) are interacting within these scales.

PKS 0745−191.—Clumpy arms of Hα emission spill from the center of PKS 0745−191 (Fig. 5*b*), tracing the emission from the H_2 gas (Fig. 5*a*). The brightest molecular emission occurs in the core of the galaxy and in an adjacent knot to the southeast. The H-band continuum image (Fig. 5*c*) is very smooth and shows only a few patches of dust absorption in the negative residual image (Fig. 5*d*). The most significant of the dust features extends eastward from the core and lies directly opposite a linear continuum emission component which appears to be a tiny jet. The 2 cm radio contours (Fig. 5*e*) from Baum & O'Dea (1991) show a distortion in the same scale and position angle as the putative jet feature. Distorted and extended 6 cm radio contours (Fig. 5*f*), also from Baum & O'Dea (1991), surround the core of the galaxy but exhibit no clear indications of jets or lobes. The shape of the 6 cm radio source suggests that some interaction may be occurring between the system with the dust feature and the radio source.

In Figure 7, we identify clumps of gas which are present in both the ionized and the molecular residuals, and we calculate the flux ratio of the two components for each clump in Table 6.

7. DUST EXTINCTION

The optical and near-infrared images of all three galaxies show significant dust lane features. These lanes show up as patchy or filamentary absorption against a smooth elliptical distribution of light. By fitting and dividing out the elliptical backgrounds, the quantity of absorption in each wave band can be estimated. The ratio of the absorption in any two bands provides a point on the reddening law for the dust in that system. Using this method, we show that the dust in each of these systems is consistent with a Galactic reddening law.

In the central region of NGC 1275, dusty patches significantly obscure the galaxy, and this obscuration is still quite strong at infrared wavelengths of $\sim$1.6 μm, or H band. A longer WFPC2 R-band exposure from the Hubble Data Archive provided the comparison opacity of the dust features at optical wavelengths. (This exposure saturates the central nucleus, so we did not use it to subtract continuum from the LRF image.) If the underlying stellar emission is smoothly distributed across the galaxy, the ratio of extinctions A_R and A_H could provide one point of the reddening law of the extinction. However, the emission maps created in the previous analysis revealed thick, clumpy patches of Hα emission. Therefore, optical line emission contaminates the continuum estimate of this filter, and the extinction rela-

tion derived using this filter might be suspect. For this reason, we also use archival WFPC2 data at *B* band (F450W) for the analysis of the dust lanes in NGC 1275. Our conclusions using either the *B* or the *R* data with the *H*-band data are similar.

We forced the isophotal fitting parameters (the shapes and the centroids) of the optical images to match that derived for the NICMOS F160W image, except for the normalizations. We then divided the *B*-band, *R*-band, and *H*-band images by their isophotal models to create residual images which map the dust and allow a quantitative extinction estimate in magnitudes. The residual images were binned to $\sim 0\farcs2$ resolution, and the detection limit for an absorption feature was determined to be ~ 0.03 mag at *H*-band. Assuming the relations for Galactic-type opacity (Cardelli et al. 1989) and $R_v = 3.1$, the *H*-band limit corresponds to a limit of 0.20 mag at *B*, which we use for a lower cutoff. For reference, extinction ratios for each filter pair

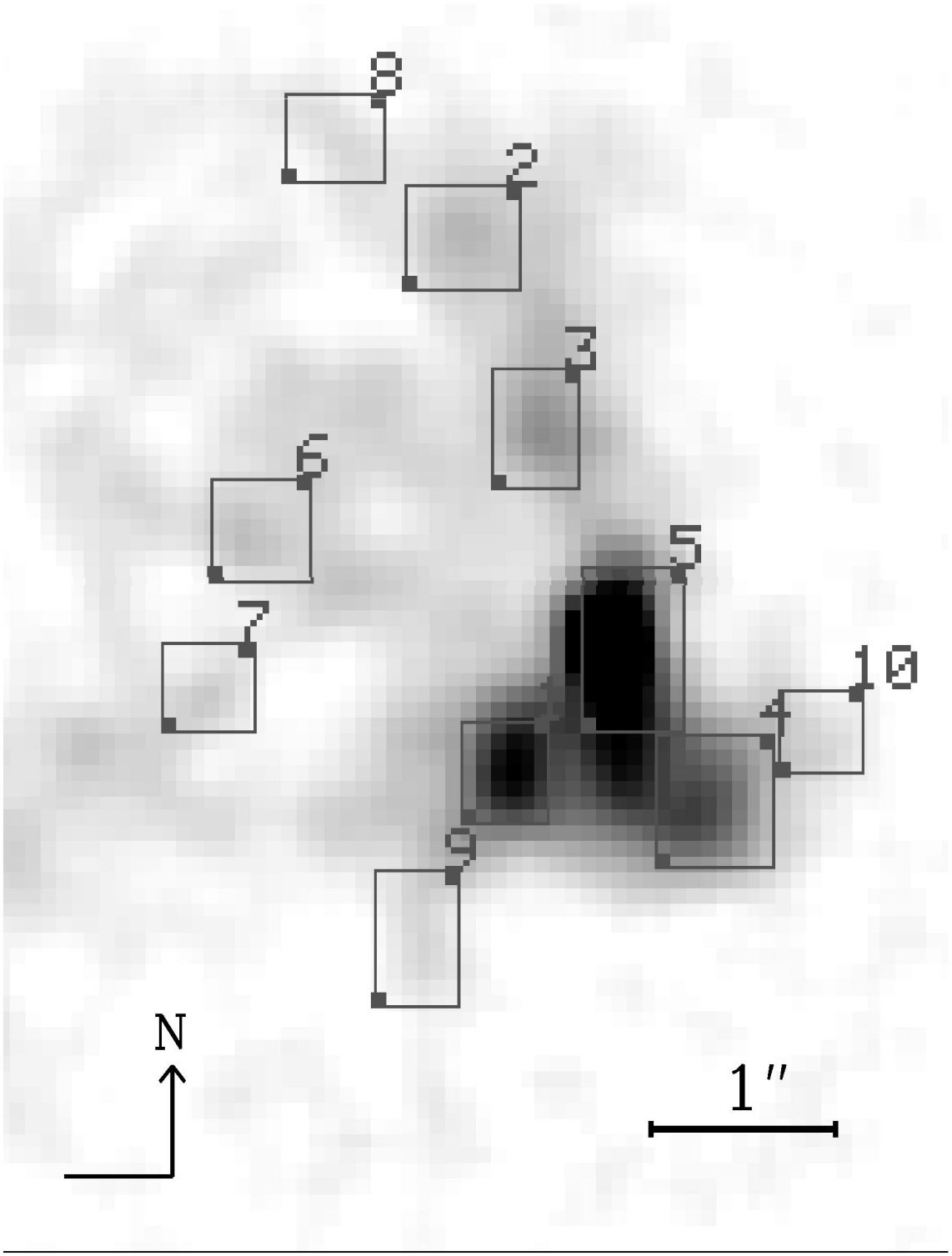

FIG. 6.—A2597 clump regions

TABLE 5

A2597 Individual Clump Fluxes

Clump	Area (arcsec^2)	H_2 (10^{-16} ergs s^{-1}cm^{-2})	Hα+[N II] (10^{-15} ergs s^{-1} cm^{-2})	[O II] (10^{-15}ergs s^{-1} cm^{-2})	H_2/(Hα+[N II])	H_2/[O II]
1[a]	0.236	2.91 ± 0.09	1.69 ± 0.02	2.42 ± 0.06	0.172 ± 0.017	0.120 ± 0.005
2	0.315	1.13 ± 0.03	1.70 ± 0.01	1.69 ± 0.04	0.066 ± 0.004	0.066 ± 0.003
3	0.270	1.47 ± 0.05	2.10 ± 0.01	1.81 ± 0.05	0.070 ± 0.003	0.081 ± 0.003
4	0.405	3.5 ± 0.1	4.71 ± 0.03	4.62 ± 0.13	0.074 ± 0.004	0.076 ± 0.003
5[a]	0.433	7.0 ± 0.4	3.79 ± 0.02	5.29 ± 0.12	0.185 ± 0.013	0.133 ± 0.008
6	0.276	0.85 ± 0.02	1.03 ± 0.06	1.31 ± 0.04	0.083 ± 0.004	0.065 ± 0.003
7	0.203	0.49 ± 0.02	0.829 ± 0.004	0.93 ± 0.02	0.059 ± 0.004	0.052 ± 0.003
8	0.236	0.43 ± 0.02	1.44 ± 0.02	1.41 ± 0.05	0.030 ± 0.003	0.031 ± 0.002
9	0.304	0.63 ± 0.03	1.28 ± 0.01	1.28 ± 0.05	0.049 ± 0.005	0.049 ± 0.003
10.....	0.203	0.52 ± 0.03	0.426 ± 0.006	1.04 ± 0.03	0.122 ± 0.013	0.050 ± 0.003

[a] Regions with heavy dust obscuration which probably affects at least the observed optical line fluxes.

were calculated using the infrared and optical Galactic extinction relations with the mean filter wavelength (0.452, 0.687, and 1.593 μm at B, R, and H). This gives the results $A_{F450W}/A_{F702W} = 1.65$, $A_{F702W}/A_{F160W} = 4.07$, and $A_{F450W}/A_{F160W} = 6.73$.

The image in Figure 8 (*upper left*) is a ratio map of the extinction magnitudes for the residual B- and H-band images, where black represents Galactic-type opacities ($A_B/A_H = 6.7$), gray scale indicates where the ratio is less than Galactic, and white indicates regions with no dust in

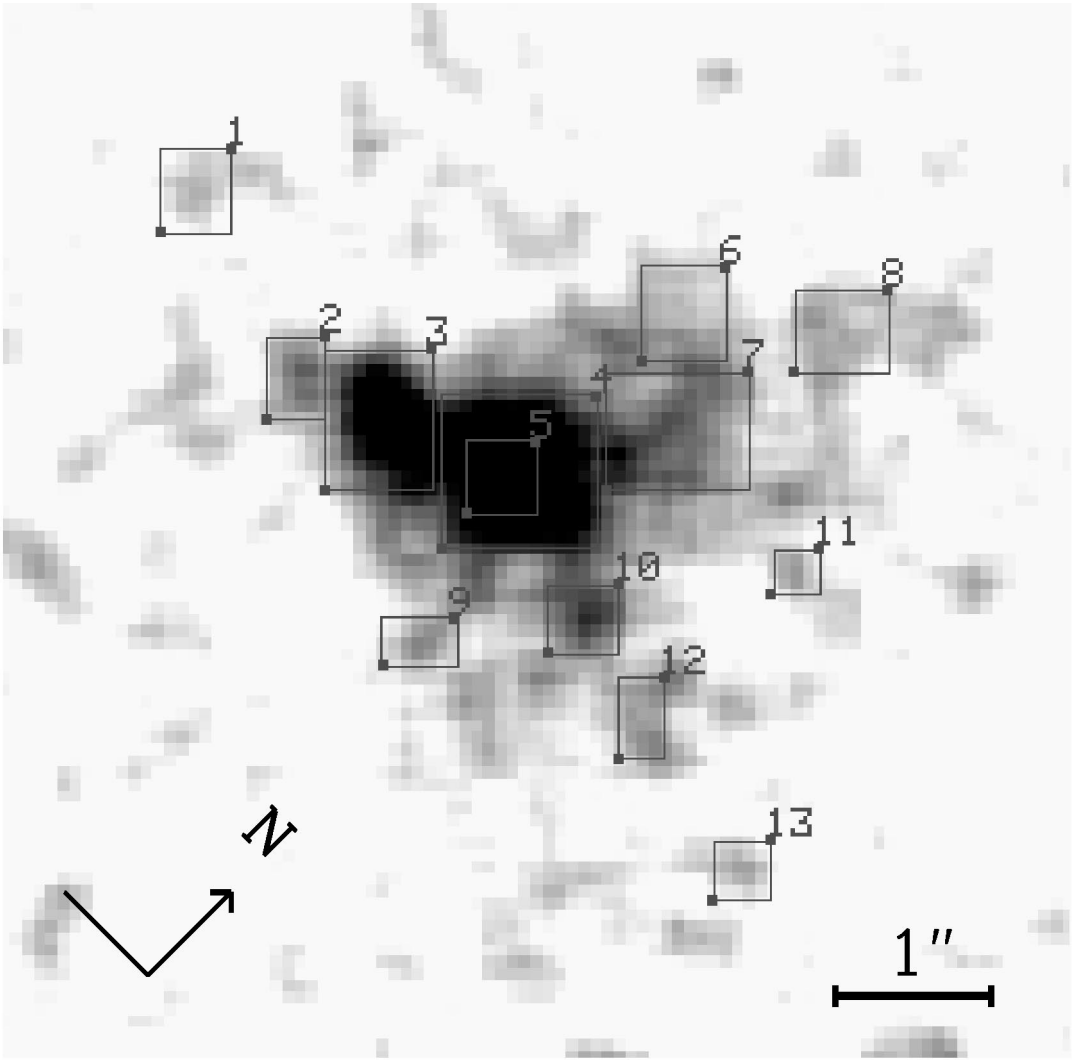

Fig. 7.—PKS 0745−191 clump regions

TABLE 6

PKS 0745−191 Clump Fluxes

Clump	Area (arcsec^2)	H_2 (10^{-16} ergs s^{-1}cm^{-2})	Hα+[N II] (10^{-16} ergs s^{-1}cm^{-2})	H_2/(Hα+[N II])
1	0.315	0.93 ± 0.06	4.78 ± 0.15	0.194 ± 0.015
2	0.270	1.25 ± 0.08	10.7 ± 0.33	0.117 ± 0.008
3	0.731	7.2 ± 0.3	52.0 ± 1.7	0.139 ± 0.008
4	1.100	16.7 ± 0.8	230 ± 14	0.073 ± 0.006
5	0.276	7.6 ± 0.5	123 ± 8	0.062 ± 0.005
6	0.405	1.77 ± 0.06	12.6 ± 0.3	0.141 ± 0.006
7	0.804	5.06 ± 0.12	42.2 ± 0.8	0.120 ± 0.003
8	0.405	1.92 ± 0.06	12.2 ± 0.3	0.157 ± 0.006
9	0.197	0.59 ± 0.05	6.78 ± 0.2	0.087 ± 0.008
10.....	0.276	1.60 ± 0.07	13.1 ± 0.3	0.122 ± 0.006
11.....	0.141	0.47 ± 0.04	6.84 ± 0.10	0.069 ± 0.006
12.....	0.225	1.08 ± 0.04	12.0 ± 0.25	0.09 ± 0.004
13.....	0.203	0.70 ± 0.05	5.4 ± 0.2	0.129 ± 0.010

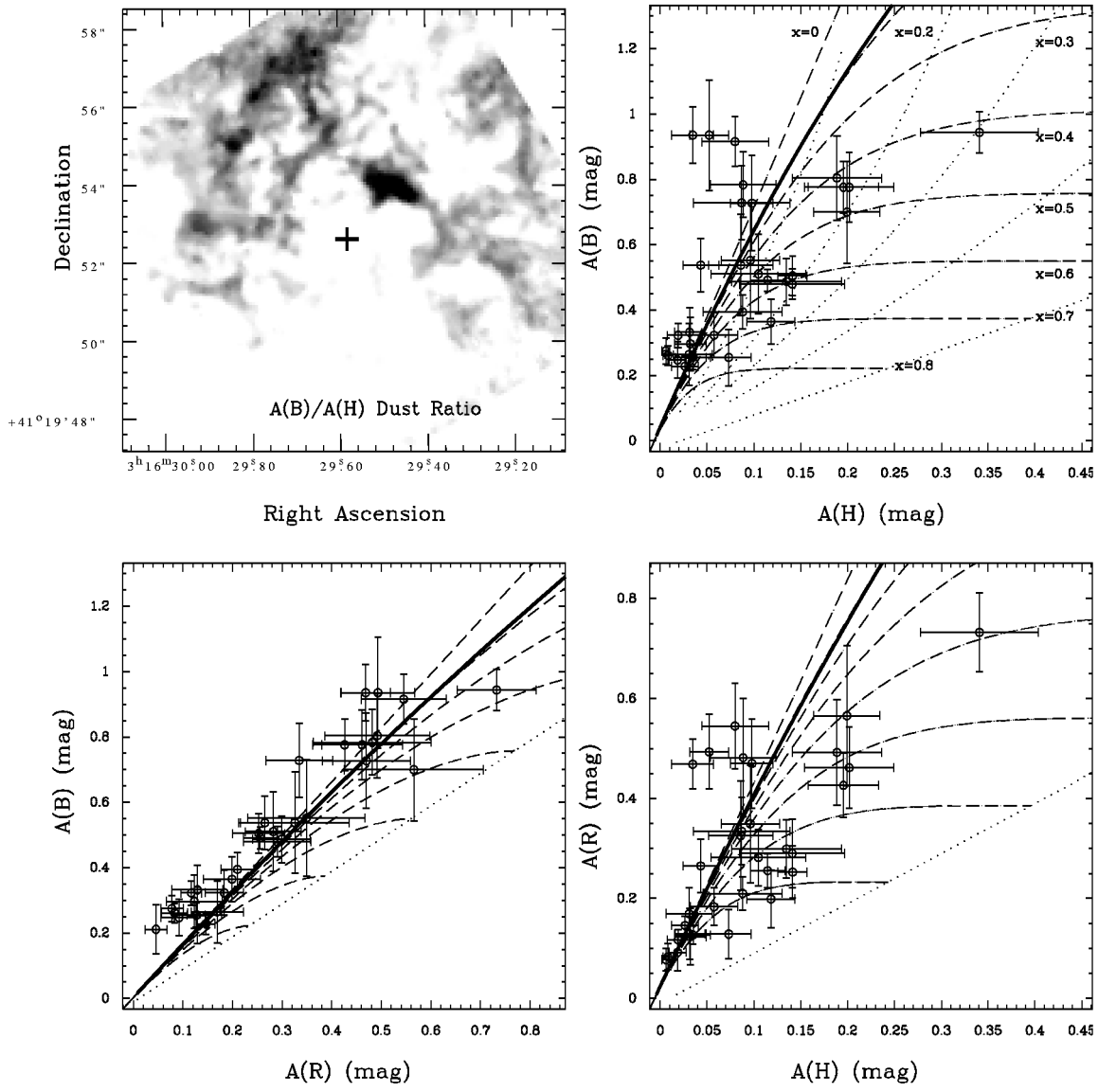

Fig. 8.—Dust in NGC 1275. (*Upper left*) Ratio of extinction maps in *B* band and *H* band. Black indicates a Galactic-normal reddening ($A_B/A_H = 6.7$); white indicates $A_B/A_H = 1.0$ (either no or gray extinction). Cross marks center of galaxy. (Note that Fig. 3*d* maps absorption features themselves.) (*Upper right*) A_B vs. A_H extinction. (*Lower left*) A_B vs. A_R. A_R estimates are contaminated by filamentary [N II] + Hα emission. (*Lower right*) A_R vs. A_H. Data points are means and their rms deviations in 0.″375 × 0.″375 regions. Bold line is expected relation for uniform mixture of stars and dust. Dashed lines plot relation when dust is geometrically thin, where x is the fraction of light in front of the dust. (See text for details.)

either filter. We plot the measured extinction in two ways in Figure 8 (*upper right*): for each dusty pixel in the image and as a median extinction value, calculated in 0.1 mag bins. Two simple models described in Walterbos & Kennicutt (1988) have been overplotted onto the data. The first of these (Model 1, bold line) shows the expected relation for a uniform mixture of stars and dust. The second model (Model 2) assumes that the dust lane is geometrically thin and that the dust is embedded in a stellar disk, where x is the fraction of light in front of the dust. Dashed lines represent varying values of x (0.0–0.8) and dotted lines represent varying values of τ_h (0.2, 0.4, 0.6, 1.0, ∞). For infinite optical depth, the expected extinction in the two colors is equal, since only light from sources in front of the dust would be detected.

In Figure 8 (*upper right*), we see that Model 1 is an approximation to only some of the data. Model 2 fits some of the points in a range of $0.4 < x < 0.8$ and $\tau_h < 0.4$. In the image, these points correspond mainly to the large dust feature northeast of the galaxy's center, where the 1.6 μm opacity is the highest (see Fig. 3*d*). The correspondence to Model 2 implies that the dust in the central few arcseconds of NGC 1275 is well mixed with the stars, but not in a uniform manner. Optically thick patches appear to be intermixed with regions showing Galactic-type opacities. These regions are the darkest regions in the gray scale (Fig. 8, *upper left*).

In the lower panels of Figure 8, we plot the A_B versus A_R and A_R versus A_H extinctions. Contamination due to optical line emission at R band or B band changes the intercept of the color plots. Certainly, some contamination occurs in the broad R-band filter. Assuming that contamination is 7%, this effect moves data points in Figure 8 (*lower left*) to the right and in Figure 8 (*lower right*) up by 0.07 mag. A straight-line fit to the A_B versus A_R extinction, allowing for error bars in both directions, reveals a slope of 1.45 ± 0.13, somewhat less steep than a simple screen of Galactic dust but consistent with some mixing between stars and dust. A formal intercept of 0.10 ± 0.03 mag is found, which is consistent with our estimate of the contamination in R. Three outlying points, with apparently high extinction in the blue band but very little extinction in the R and H bands, lie very near a strong dust feature just northeast of the center of the image. Inside this feature lies a very red star cluster (perhaps a globular cluster) which is strongly absorbed at B but is just visible in H.

The most significant result to be noted from the absorption comparison plots is that the slope of the extinction relation appears to be either the same as, or less steep than, that of a Galactic extinction relation, which is consistent with a heterogeneous mix of stars and Galactic dust. Therefore, we see very little evidence for an unusual dust law in NGC 1275. There is a significant amount of dust, which we can see in distinct features even at 1.6 μm, but the reddening is consistent with that of normal Galactic-style dust. The NGC 1275/Perseus observations do not show the unusually steep slope for the absorption ratios as measured for Abell 1795 by Pinkney et al. (1996).

In Abell 2597, spectroscopic determination of A_R from the Balmer line decrement and the assumption of a standard reddening law in the central 2″ provided an estimate of an absorption of $A_R \sim 1$ (Voit & Donahue 1997). Estimating the dust absorption and reddening from existing *HST* imaging for Abell 2597 is problematic. We have no line-free optical continuum image for Abell 2597. For the strongest absorption feature in the image, a triangular aperture wedged alongside the nucleus, $A_R \sim 0.10 \pm 0.01$ mag and $A_H = 0.009 \pm 0.002$ mag, giving a ratio of 10.7 ± 2.8. This ratio, however, must be suspect. The red filter measurement is strongly contaminated by line emission from the Hα + [N II] complex (so much so that we can use the image to estimate Hα fluxes). The red "absorption" of this feature may be wrong because our technique for estimating it is not robust to significant amounts of structure, which certainly exists nearby the nucleus of A2597. The observed ratio in this small region is nonetheless consistent with what is expected from optically thin Galactic-style dust, but high-resolution, high-quality, pure optical continuum observations or deep optical spectroscopy are needed for a reliable measurement of dust.

The continuum (F439W) image of PKS 0745−191 also does not permit a very accurate measure of the color sensitivity of the absorption in the single dust feature in that source. In the dust bar feature just west of the nucleus, $A_B = 0.16 \pm 0.04$ and $A_H = 0.05 \pm 0.01$ mag, corresponding to a ratio 2.9 ± 1.1, less than the expected Galactic ratio of 6.7, but consistent with a dust slab where 80% of the observed starlight lies in front of it.

In summary, we have unambiguously detected the absorption of dust features in all three galaxies. For NGC 1275, we have extensive measurements for the prominent dust features in that system, while for A2597 and PKS 0745−191, the estimates were possible for only a single feature in each system. For all three sources, the ratios of the optical to the infrared absorption are consistent with Galactic reddening. The dust absorption is consistent with that of rather thick, normal dust clouds lying behind foreground stars.

8. ORIGINS OF THE GAS

In order to emit in the 1–0 $S(1)$ or 1–0 $S(3)$ vibrational transition line, molecular hydrogen must be vibrationally excited. If it is excited collisionally, it must be relatively warm (1000–2000 K). To infer anything more about this gas, we would like to know where it came from and how it is heated. In the following section we discuss the possible origins of the gas and of the gas morphologies.

8.1. *The Molecular Gas Is Not Part of a Cooling Flow*

The molecular emission lines are far too bright to be from cooling gas (Jaffe & Bremer 1997). If molecular line emission is responsible for radiating energy from a cooling flow as the gas cools through the temperature 2000 K, the fraction of cooling expected from a single H_2 infrared line is about $\eta = 2\%$–10%. Estimating the mass cooling rate by

$$\dot{M} = \frac{m_{H_2}\Phi}{\eta}, \tag{2}$$

where m_{H_2} is the mass of a hydrogen molecule and Φ is the line luminosity in photons per second, we find a mass cooling rate inside the central 2″ of tens of thousands of solar masses per year, 2 orders of magnitude larger than the *total* cooling flow rates over an entire cluster (Table 1). Specifically, the mass cooling rates implied for NGC 1275, A2597, and PKS 0745−191 would be 18,000, 16,000, and 29,000 $h^{-2} M_\odot$ yr^{-1}, respectively.

One possible source of the gas, however, could be the intracluster medium (ICM). It is difficult to imagine scenarios where molecule formation would occur readily in the cores of cluster cooling flows (Voit & Donahue 1995), although the possibility has been explored (Ferland, Fabian, & Johnstone 1994). Molecular hydrogen formation occurs most readily when dust is present (although there are formation scenarios where dust is not required). Since dust should not last long in the hot ICM, we do not expect molecular hydrogen to form in gas that has condensed out of the ICM. Furthermore, the large energy density in X-rays will inhibit both dust and molecule formation (Voit & Donahue 1995). Therefore, this molecular hydrogen is unlikely to be the end product or direct evidence of a cooling flow.

8.2. *Morphologies of the Dust and Optical and Infrared Emission-Line Gas*

The emission-line morphologies in these clusters indicate that the H_2 gas is closely related to the Hα-emitting gas. The emission-line filaments of H_2 align nearly exactly with the emission-line filaments of Hα. We are unable to tell whether the correspondence extends to lower surface brightnesses, but the highest surface brightness features seem to overlap substantially. The correspondence of the optical and infrared emission-line filament structures suggests, but does not demand, that the heating mechanisms might also be related.

The filaments themselves are concentrated in the central region in bright fuzzy blobs and extend away from the nucleus in delicate tendrils that seem to surround cavities that may have been evacuated by radio sources. Some of the filaments have knots which could be simply brighter parts of the filaments or H II regions which are photoionized by stars. The structure of the extended filament system is suggestive of shocks; however, we know from nuclear emission-line spectroscopy of A2597 (Voit & Donahue 1997) and from stellar continuum analysis of central galaxies in cluster cooling flows (Cardiel et al. 1998) that hot stars play a significant role in the optical line emission from these galaxies.

The arcsecond-scale radio sources in both Abell 2597 and PKS 0745−191, and, to a limited extent, in NGC 1275, appear to be interacting with the atomic and vibrationally excited molecular gas. The radio plasma in these galaxies seems to be affecting and is affected by the atomic and molecular gas.

The dust absorption features of these three galaxies do not align with the emission-line filaments, although there is some overlap. The dust features tend to be elongated in the same direction as the emission-line feature, and in some cases, the dust lanes run alongside the emission-line filaments. The conclusion of this morphological observation is that while the emission-line gas itself is known to be dusty based on significant calcium depletion—that is, no or very little [Ca II] emission has been observed (Donahue & Voit 1993)—there is certainly dusty gas which is not associated with the emission-line filaments and may be quite distinct from them. This dust seems to be quite normal in NGC 1275, A2597, and PKS 0745−191, as we showed in § 7. Sparks et al. (1993, 1989) discovered normal Galactic-style dust in M87 and NGC 4696 (Centaurus) respectively. (In these systems, the emission-line gas and the dust appear to be cospatial, at least on arcsecond scales.) If the dust properties are consistent with those of Galactic dust, it is unlikely that the dust has been processed by X-rays or is a by-product of any process whereby the nebular or dusty gas condenses from the hot gas.

It is therefore unlikely that the dust, the ionized emission-line gas, and by association, the warm molecular gas, originated as intracluster material at X-ray–emitting temperatures. Sparks et al. (1989, 1993) have speculated that a merger event provided the gas, citing the coherent filamentary structure, the quantity of dust, and the angular momentum of the emission-line gas as evidence.

9. HEATING THE GAS

Our observations allow us to test hypotheses about how the molecular gas might be heated. Vibrationally excited molecular hydrogen is present in both active galaxies and in starburst galaxies. Therefore, both stars and AGNs can vibrationally excite molecular hydrogen. We note that the exact physical process responsible for the excitation is not clear even for starburst and active galaxies.

The molecular emission from NGC 1275 is likely to be dominated by its AGN, but that of Abell 2597 and PKS 0745−191 is not. Therefore our discussion in this paper will focus on testing explanations for what is heating the molecular gas in these two systems. The pointlike morphology of the H_2 emission of NGC 1275 suggests that it is probably related to nuclear activity. Other Seyfert galaxies show nuclear infrared H_2 emission on small size scales. NICMOS imaging of nearby Seyfert galaxies by Quillen et al. (1999) revealed resolved or extended 2 μm hydrogen line emission from six out of 10 Seyfert galaxies, coincident with the Hα+[N II] line emission, and on much smaller physical scales than we observe in Abell 2597 and PKS 0745−191 (several hundred parsecs rather than a few kiloparsecs, as observed in A2597 and PKS 0745−191). The H_2-to-Hα line ratios observed by Quillen et al. (1999) are similar to that of NGC 1275.

In contrast, the H_2-to-Hα ratios in both the nuclei and in the off-nuclear filaments in A2597 and PKS 0745−191 are unusually high, even with the significant uncertainties that are incurred in correcting for [N II] emission and other systematics. Extinction of Hα relative to H_2 may be occurring, and this certainly appears to be the case just eastward of the A2597 nucleus, where there is a significant dust feature, H_2 emission, and no Hα. But global source-wide extinction does not appear to be a significant factor in producing the high ratios. (Observations of A2597 Balmer lines suggest reddening consistent with $A_v \sim 1$; Voit & Donahue 1997.)

Falcke et al. (1998) finds an H_2-to-Pα ratio of 0.50 for PKS 0745−191 and 2.02 for A2597. If we scale our H_2 observations by these ratios, we can compare this rough estimate of the Hα/Pα ratios to that expected for case B Hα/Pα. For $T_e = 10^4$ K, Osterbrock (1989) predicts 8.3 (see also Brocklehurst 1971), and the ratio ranges between 7.5 and 9.7 for $T_e = 5000$–20,000 K. Our observed nuclear Hα/Pα ratios are 8.7 ± 1.8 for A2597 and 2.9 ± 0.6 for PKS 0745−191. The ratio in A2597 is consistent with case B recombination with little or no extinction. We note that a far more reliable analysis of the Balmer series for a single deep long-slit observation of A2597 by Voit & Donahue (1997) obtains $A_V \sim 1$, without the aperture uncertainties inherent in this comparison. The Hα/Pα ratio in PKS 0745-191 is consistent with a differential absorption between Hα

and Pα of only 50%–60% at the wavelength of Hα, corresponding to a modest $A_V \sim 1$ (Hill, Goodrich, & Depoy 1996; Seaton 1979). We conclude that the internal extinction of the emission-line gas is not huge, $A_V \sim 1$ for both sources.

We will thus use the following three pieces of evidence to test the physical models, supplementing with observations at UV, radio, and X-ray wavelengths as appropriate:

1. The morphological similarity between the emission-line gas in the optical and in the near-infrared for A2597 and PKS 0745.
2. The unusually high intrinsic ratios of H_2 emission to Hα emission, both globally and locally in A2597 and PKS 0745.
3. The relatively intense surface brightness of H_2 emission as measured locally in A2597 and PKS 0745.

9.1. *X-Ray Photoelectric Heating, Conduction, and Mixing Layers*

X-rays can quickly be ruled out as a viable universal source of heat for the near-infrared filaments in at least one of the clusters, Abell 2597. X-ray photoelectric heating can excite H_2 vibrational lines deep within the cloud. It is a process which can reproduce the H_2-to-Hα line ratios, given a sufficient column depth of hydrogen. X-ray irradiation and heating will also destroy H_2, but warm ($T \sim 1000$–2000 K) H_2 radiates so efficiently in the 1–0 $S(1)$ line that only a small column of H_2 ($\sim 3 \times 10^{18}$ cm^{-2} out of a total hydrogen column of $\sim 10^{21}$ cm^{-2}, a molecular fraction of only $\sim 3 \times 10^{-3}$) is required to produce the observed surface brightnesses.

We used archival *ROSAT* HRI images to assess the local X-ray flux in each source. The *ROSAT* HRI detector acquires a simple image (no spectra) of an X-ray source between 0.2 and 2.0 keV, with a spatial resolution of $\sim 4''$. The 0.5–2.0 keV X-ray luminosity as measured from HRI imaging within a circular aperture of $r = 8''$ and a $4'' \times 4''$ box for each target is listed in Table 7. We corrected the observed X-ray luminosities to bolometric X-ray luminosities by assuming the temperatures and Galactic columns (Table 1) and 30% solar metallicities. The ratio of the bolometric X-ray flux to the H_2 line flux shows a wide variation, from 7 for A2597 to 400 for PKS 0745. We did not attempt to correct the bolometric X-ray flux–to–H_2 line flux ratios for the different sizes of apertures in the two measurements. (Higher spatial resolution images from *Chandra* would provide a better direct comparison, of course.)

For gas that has been heated to ~ 2000 K, the 1–0 $S(1)$ line emits about 0.5% of the absorbed X-ray luminosity. This line is responsible for about 10% of the total H_2 line flux, which is in turn responsible for about 10% of the total cooling in an X-ray–heated cloud (e.g., Lepp & McCray 1983). About 50% of the absorbed X-ray energy goes into heating the gas (in contrast to photodissociation regions, where the efficiency is closer to 0.1%). Typical X-ray/$S(1)$ ratios obtained from X-ray irradiation models (Maloney, Hollenbach, & Tielens 1996) are around 2000, since only about 10% of the incident flux is absorbed by clouds with $\sim 10^{22}$ cm^{-2} columns. The ratio can be smaller for a very steep incident spectrum.

In the case of NGC 1275, the AGN may be supplying a significant fraction of the central X-ray luminosity, and therefore, with a steeper spectral component, the predicted ratio between X-ray and 1–0 $S(1)$ flux is lower and closer to that observed. But for Abell 2597, significant X-ray heating of the H_2 gas seems highly unlikely given the absence of a significant intrinsic absorption column. Its L_x/L_{H_2} ratio of 7 within the $4'' \times 4''$ aperture is far too low for X-ray heating to be energetically possible. PKS 0745−191 is closer to the Galactic plane, and therefore its Galactic column and the uncertainty on its intrinsic column is higher. If PKS 0745-191 has significant intrinsic absorption, X-ray heating of its H_2 gas is remotely possible but not likely. High S/N *Chandra* CCD observations would have sufficient angular resolution to test whether there is significant intrinsic absorption of X-rays, using spectra from only the central few arcseconds.

Based on relative observed fluxes, while the local X-ray flux compared to the optical and molecular emission-line flux is insufficient to produce the line emission by X-ray heating for Abell 2597, photoelectric heating of the molecular gas by X-rays is remotely feasible in the cluster PKS 0745−191. To explore what Hα/H_2 $S(1)$ line ratios one might expect from X-ray–heated gas, we have constructed a constant-pressure model, using the methods described in Maloney et al. (1996), where $P/k = 10^8$ cm^{-3} K and the incident spectrum is flat (in f_ν), with a cutoff at 8 keV to mimic a thermal spectrum, and a total cloud column of 1.5×10^{22} cm^{-2}. A warm ($T \sim 8000$ K), weakly ionized ($x_e \sim 0.01$–0.1) atomic zone is produced near the surface; with increasing column density into the slab, the gas undergoes a transition to a molecular phase. The ratio of Hα to $S(1)$ (including Hα from the warm atomic zone only) is about 4; including the Hα contribution from the highly ionized layer at the surface of the slab raises the ratio to 8, comparable to the ratios we observe in these clusters.

We note that the Hα/$S(1)$ ratio is sensitive to the slope of the continuum below a few hundred electron volts and the total cloud column density. If the spectrum is much softer than what we assume (that is, if the number of photons between 13.6 and 100 eV is significantly larger than the number of photons between 1 and 8 keV), the Hα contribution from the fully ionized layer could be much larger. Also, if the total column density of the cloud is 5×10^{21} cm^{-2} rather than 1.5×10^{22} cm^{-2}, the molecular gas column decreases and the predicted Hα-to-$S(1)$ ratio increases to 80.

TABLE 7

X-RAY MEASUREMENTS FROM *ROSAT* HRI

Name	$L_{0.5-2.0\mathrm{keV}}$ ($r < 8''$) (h^{-2} ergs s^{-1})	$L_{0.5-2.0\mathrm{keV}}$ ($4'' \times 4''$ box) (h^{-2} ergs s^{-1})	Bolometric Correction	L_{bol}/L_{H_2}
NGC 1275.....	1×10^{42}	1.8×10^{41}	4.22	23
A2597	5×10^{41}	5.5×10^{40}	4.12	8
PKS 0745	2×10^{43}	2.5×10^{42}	8.01	360

Therefore, for X-ray–heated gas, the predicted Hα-to-$S(1)$ line ratios can be tuned to a range of values consistent with what we observe. If these clouds are X-ray heated, therefore, the incident spectrum is probably rather flat (consistent with thermal bremsstrahlung), and the clouds must be thick ($>10^{22}$ cm^{-2}). But, the mechanism is energetically unlikely based on ratios of the observed X-ray luminosities to $S(1)$ emission-line luminosities, especially for Abell 2597.

Mechanisms with physical processes similar to those which accompany X-ray heating, but with slightly different sources of energy, have been postulated as energy sources for the optical filaments. Conduction (Sparks et al. 1989) and irradiation by mixing layers (Begelman & Fabian 1990) are models which are not as easily tested by the data in hand, although the lack of coronal line emission (Donahue & Stocke 1994; Yan & Cohen 1995) strongly constrains the parameters of mixing layer models, which rely on local X-ray– and UV-emitting gas to heat the filaments.

All three models, conduction, mixing layer, and direct X-ray heating (Voit & Donahue 1990), tap into the thermal energy of the ICM, but only conduction can draw from the vast thermal reservoir not local to the filaments. Determining whether conduction or irradiation by mixing layers could generate sufficient luminosity to explain the observations depends on assumptions about filament geometry, the electron density of the ICM, and, to some extent, the magnetic field strength and structure. For example, a conduction model with modest assumptions of electron densities of $n_e \sim 0.5$ cm^{-3}, $T_e \sim 10^7$ K, filament surface area that is 3 times the projected area, and a conduction flux which is 1% the classic saturated flux, predicts there is sufficient energy in these systems to power the optical and infrared line luminosity of the filaments. The line ratios of H_2 to Hα have not been computed for such models but are likely to be similar to those we derive here for direct irradiation of thick columns of hydrogen by the X-ray–emitting ICM. Therefore, we cannot rule out conduction or mixing layers as a possible energy source for the molecular emission-line filaments.

9.2. *Shocks*

The filamentary morphology of the emission is suggestive of shock heating, but not proof. The observed optical line emission from the central 2″ of A2597 is inconsistent with shocks being the primary source of the energy (Voit & Donahue 1997), but the molecular emission could arise from a separate process. In the next few paragraphs, we will examine the implications of our observations in the context of shock models (Hollenbach & McKee 1989).

The intrinsic surface brightnesses predicted by the shock models suggest that the preshock densities are between 10^3 and 10^4 cm^{-3} and possibly up to 10^5 cm^{-3} for the brightest Hα systems. If our line of sight passes through multiple shock fronts, the observed surface brightness exceeds the true surface brightness of the working surface of any given shock, and the true preshock densities could be somewhat lower.

Fast shocks produce Hα/H_2 line ratios that are significantly higher than observed, as fast shocks dissociate H_2 and have thick ionization regions. The observed Hα/H_2 ratios span 1.5–10 in A2597 and 2–7 in PKS 0745−191 (the ratios in PKS 0745−191 are a factor of 2 higher if Hα is significantly attenuated by dust). For preshock densities of 10^3–10^4 cm^{-3}, the observed ratios constrain the shock velocities to less than 50 and less than 40 km s^{-1}, respectively (Fig. 9). If the Hα production is supplemented by stellar photoionization or any other possible source, the Hα/H_2 ratio from a putative shock is even lower, and thus the velocities of the shocks must be lower.

If low-velocity shocks are producing the H_2 emission, the amount of matter being processed by these shocks is enormous, on the order of 10,000–100,000 $M_\odot$ of shocked gas per year. Also, the turbulent velocities must be significantly greater than the shock velocities in order for such slow shocks to be consistent with the velocity widths of the infrared and optical emission lines ($v_{\rm FWHM} \sim 300$–500 km s^{-1}.) However, models of radio lobes and the shocks propagating into a uniform medium suggest that in some cases, one

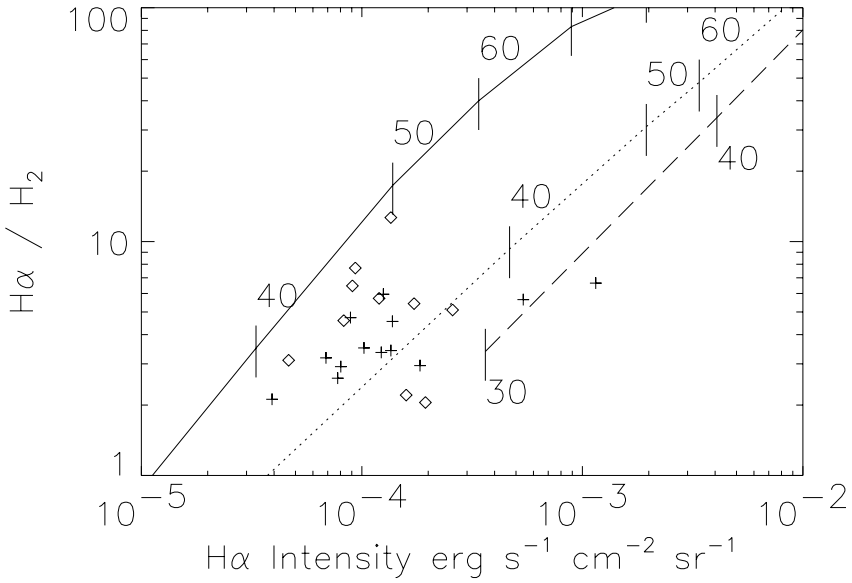

FIG. 9.—Ratio of Hα and H_2 emission-line flux compared to estimated Hα surface brightness of knots in Abell 2597 (*diamonds*) and PKS 0745−191 (*crosses*). Lines plot line ratios and surface brightness predicted by shock models (Hollenbach & McKee 1989), with $v_{\rm shock} = 40$–60 km s^{-1} labeled. Solid line is for preshock density of $n_0 = 10^3$ cm^{-3}, dotted line is for $n_0 = 10^4$ cm^{-3}, and dashed line is for $n_0 = 10^5$ cm^{-3}.

might predict extremely slow shocks if the preshock gas is very dense, while the plume of material behind the shock may emit substantially broader optical emission lines (A. M. Koekemoer, private communication.)

9.3. *UV Fluorescence and Star Formation*

9.3.1. *Star Formation,* Hα, *and Far-Infrared Emission*

If the Hα in the central 2″ in all three galaxies is generated by star formation, we can infer a lower limit for steady star formation (a lower limit because the Hα could be absorbed by dust) for the three targets of 2–5 $h^{-2}\ M_{\odot}\ \mathrm{yr}^{-1}$, scaling tabulated models from Gehrz, Sramek, & Weedman (1983). We explored a standard model with initial mass function slopes of $\alpha = 3.5$ and initial stellar masses between 6–25 $M_{\odot}$. (We note that these star formation rates fall 1–2 orders of magnitude short of that required to explain the fate of the mass inferred from X-ray observations to cool from the intracluster media.) Much of the radiation generated by star formation in dusty environments is reemitted in the far-infrared. The bolometric (infrared) luminosities predicted from these models, as required to generate the observed Hα luminosities, are (8–23) $\times\ 10^{43}$ ergs s^{-1}, where the predicted luminosity of NGC 1275 is $8 \times 10^{43} h^{-2}$ ergs s^{-1}, A2597 is $1 \times 10^{44} h^{-2}$ ergs s^{-1}, and PKS 0745−191 is $2 \times 10^{44} h^{-2}$ ergs s^{-1}, consistent with and not too far below the 2 σ *IRAS* upper limits for 4′ diameter apertures centered on Abell 2597 and PKS 0745 (Wise et al. 1993). NGC 1275 is a far-infrared (FIR) source (Moshir et al. 1990) with νL_{ν} at 60 μm of $1.2 \times 10^{44} h^{-2}$ ergs s^{-1}. (νL_{ν} of a galaxy at 60 μm is within a factor of several of the total FIR luminosity of the galaxy.) FIR luminosities νL_{ν} of A2597 and PKS 0745-191 have nonrestrictive upper limits of less than $2 \times 10^{44}\ h^{-2}$ ergs s^{-1} and less than $7 \times 10^{44}\ h^{-2}$ erg s^{-1}, respectively (Wise et al. 1993). The far-infrared observations of these galaxies are consistent with the conjecture that all of the Hα may be produced as a result of star formation. We will next test whether this assumption is consistent with the near-infrared observations.

9.3.2. *UV Fluorescence,* Hα, *and* H_2 *Emission*

If the emission is powered by UV fluorescence, the vibrational excitation states are maintained indirectly by absorption of ultraviolet starlight in the Lyman and Werner band systems, followed by fluorescence (e.g., Black & van Dishoeck 1987, hereafter BvD87). We can infer the intrinsic UV intensity by extrapolating from the ionizing flux required to produce the Hα photons to the UV flux that would be available to excite the vibrational states of H_2. If the Hα emission arises from photoionization, one can estimate the ionizing flux ($\lambda < 912$ Å) required to produce it. If these same photoionizing sources also produce the 1100–912 Å photons, then with some assumptions about the shape of the incident spectrum, one can estimate the local intensity of 1100–912 Å flux, which excites the vibrational transitions of H_2 gas.

For UV photoionization, 0.45 Hα photons emerge for every ionizing photon absorbed, and ∼0.2% of the incident UV energy between 1130 and 912 Å emerges in a single strong H_2 line (this efficiency ranges between 0.06% and 0.3%; BvD87). Then, a typical power-law spectrum for an AGN produces an $\mathrm{H}\alpha/\mathrm{H}_2$ ratio of ∼80 (60–300), assuming $s = 0.86$ longward of 912 Å and $s = 1.8$ shortward of 912 Å, where $f_{\nu} \propto \nu^{-s}$ (e.g., Shull et al. 1999). An ionizing/UV background dominated by stellar sources can be approximated by inserting a break at 912 Å. A spectrum with a break factor of $\sim 100 b_{100}$, where $b_{100} = 1$, typical of Galactic UV sources, generates significantly lower $\mathrm{H}\alpha/\mathrm{H}_2$ ratios of $\sim 3\text{–}0.5/b_{100}$, closer to what we observe.

We compare the observed UV flux to that required to produce the H_2 emission, or the H_2 and Hα emission, and derive the implied extinction. *IUE* archival spectra show UV continua between 11 and 13.6 eV for all three targets. The UV continuum emission from these sources is very compact and essentially unresolved by *IUE*, implying an extent less than 3″. In A2597 and PKS 0745−191, the UV flux at a rest wavelength of about 1100 Å is $F_{\lambda} \sim 10^{-15}$ ergs $\mathrm{s}^{-1}\mathrm{cm}^{-2}\ \text{Å}^{-1}$; thus the luminosity per unit wavelength is $\sim 10^{39}$ ergs $\mathrm{s}^{-1}\ \text{Å}^{-1}$. (For NGC 1275, the flux of 10^{-14} ergs $\mathrm{s}^{-1}\mathrm{cm}^{-2}\ \text{Å}^{-1}$ translates to a specific luminosity of a few times 10^{39} ergs $\mathrm{s}^{-1}\ \text{Å}^{-1}$.)

Using the same spectral shape from Shull et al. (1999) and a break factor of 100, the observed fluxes implied by the Hα luminosities from the central $r = 2''$ aperture are $\sim 5 \times 10^{-14}$ ergs $\mathrm{s}^{-1}\ \mathrm{cm}^{-2}\ \text{Å}^{-1}$. These fluxes are consistent with the *IUE* fluxes if $A_V \sim 1.1\text{–}1.2$ (Seaton 1979).

We can also compare the H_2 surface brightness to the lower limit of the UV surface brightness, as estimated from *IUE* observations. BvD87 define the dimensionless quantity I_{UV} in their models as $I_{\mathrm{UV}} = I/4.76 \times 10^{-5}$ ergs $\mathrm{s}^{-1}\ \mathrm{cm}^{-2}\ \mathrm{sr}^{-1}$ between 912 and 1130 Å. The observed I_{UV} in a 3″ × 3″ aperture by this definition is ∼30 for A2597 and PKS 0745−191, including a $(1+z)^4$ surface brightness correction. $I_{S(1)}$ ranges from 10^{-4} to 10^{-5} ergs $\mathrm{s}^{-1}\ \mathrm{cm}^{-2}\ \mathrm{sr}^{-1}$ in A2597 (values from Table 5), twice those values in PKS 0745−191 (Table 6). In fluorescent excitation models, a single bright line of H_2 represents about 0.015 of the total amount of infrared line emission, so that $I_{\mathrm{IR}} \sim I_{S(1)}/0.015 \sim 10^{-2}\text{–}10^{-3}$ ergs $\mathrm{s}^{-1}\ \mathrm{cm}^{-2}\ \mathrm{sr}^{-1}$. The I_{UV} required to produce such a surface brightness is 100–1000, with a minimum total hydrogen density of 1000–3000 cm^{-3} (BvD87, Fig. 5). A dust screen with an A_V of only ∼0.5–1.1 mag from Galactic dust, corresponding to a UV extinction factor of ∼3–40 (Seaton 1979), would be required to reconcile UV continuum observations with that required to produce the H_2. The UV extinction implied is consistent with the approximate extinction derived from the Balmer line ratios from the nucleus of A2597 (Voit & Donahue 1997) and from our very rough estimates of the Hα/Pα ratios. Therefore, based on current limits on the intrinsic absorption, the observed UV flux from these objects cannot rule out UV irradiation by stars on energetic grounds.

To summarize: Based on the $\mathrm{H}\alpha/\mathrm{H}_2$ line ratios, we can rule out a power-law source of UV photons heating the gas in A2597 and PKS 0745−191, but we cannot rule out stellar UV sources. The line ratios and the energetics are consistent with the possibility that the stars are heating both the ionized gas and the vibrationally excited molecular gas.

If UV radiation is the major heating source, the fluorescence models, normalized by the amount of stellar UV photons needed to produce the Hα emission lines, predict that there should be a significant number of $v = 2$ vibrational emission lines. Such lines, like 2–1 *S*(3) (2.07 μm) and 2–1 *S*(1) (2.25 μm), do not appear in the spectra of Falcke et al. (1998), but the most significant test comes from the spectral region between 1 and 2 μm, which should be relatively rich in H_2 emission lines if UV fluorescence is important (BvD87). This line region is often obscured by atmospheric

line emission and would be easiest to observe from space (but some windows through to the ground exist for clusters at specific redshifts).

Furthermore, if UV fluorescence is the major heating source, a significant fraction of the UV will emerge as far-infrared radiation from dust. Such a scenario predicts that both Abell 2597 and PKS 0745−191 should be moderately strong FIR emitters of $\sim 10^{44}\ h^{-2}$ ergs s^{-1}, like NGC 1275. *SIRTF* observations of these sources would quickly confirm or disprove this hypothesis.

A significant consequence of UV fluorescence as the most important heating source compared to thermal- or shock-heated gas is the larger amount of molecular hydrogen required to be present to produce the emission. The difference in mass of molecular hydrogen if the gas is excited by UV and a simple thermal model with $T = 2000$ K, which would apply in the case of shocks or X-ray–heated gas, is a factor of 10^6. With Model 14 of BvD87, which is of an $n_{\rm H} = 3000$ cm^{-3} cloud with an incident UV flux of $I_{\rm UV} = 1000$, $L_{40} = L_{1-0S(1)}/10^{40}$ ergs s^{-1}, can be produced with $1.1 \times 10^9 L_{40}\ M_\odot$ of H_2, while the same amount of luminosity can be produced from only $4.1 \times 10^3 L_{40}\ M_\odot$ of H_2 heated to 2000 K (Model S2, BvD87). For the 1–0 $S(1)$ luminosities from our sources, the H_2 masses range from a few billion solar masses for the UV irradiation models to $\sim 10{,}000\ M_\odot$ for the thermal models ($\propto h^{-2}$).

For PKS 0745−191, $5 \times 10^9 h^{-2}\ M_\odot$ of H_2 is implied, which is very close to the published limits of H_2 masses from CO observations assuming the standard CO/H_2 conversions by O'Dea et al. (1994b). We note that the CO/H_2 conversion is large and likely not accurate in these environments. NGC 1275 has an uncertain H_2 mass, based on CO observations with the standard conversion, of $3 \times 10^9 h^{-2}\ M_\odot$ (Lazareff et al. 1989), very similar to the $3 \times 10^9 h^{-2}\ M_\odot$ predicted by the H_2 flux and UV excitation models. This correspondence cannot be taken too seriously because of the conversion uncertainty. Abell 2597 does not have published observations of CO emission.

10. CONCLUSIONS

We have discovered *extended* kiloparsec-scale vibrationally excited molecular hydrogen in the cores of galaxies thought to be in the centers of cooling flows in the clusters Abell 2597, PKS 0745−191, and Perseus/NGC 1275. The molecular gas was already known to be present in the nuclei, from ground-based spectroscopy, but its structure was unknown. We confirm the extended structure of molecular hydrogen seen in NGC 1275 by Krabbe et al. (2000) from the ground. The vibrationally excited molecular emission appears morphologically very similar to the ionized nebular gas in Abell 2597 and PKS 0745−191. We have also discovered dust lanes which are optically thick to 1.6 μm emission. These dust lanes do not trace the nebular gas but are also in the central few kiloparsecs. NGC 1275 has prominent dust lanes at 1.6 μm. We have shown that the dust reddening in NGC 1275 is consistent with that of Galactic dust. We have also, as a by-product of our observations, obtained H-band (1.6 μm) photometry of NGC 1275 globular clusters. We have been able to map the $H\alpha/H_2$ ratios in different positions across A2597 and PKS 0745−191.

We examine the possible sources of the vibrationally excited molecular gas, which cannot have condensed from a cooling flow. We also investigate the source of heat for the vibrationally excited molecular gas. The source of heat in NGC 1275 is likely the central AGN—we cannot discriminate between the possible processes there. For the extended emission in A2597 and PKS 0745−191, we can rule out AGN photoionization and fast shocks because the $H\alpha/H_2$ ratios are too low. We can rule out X-ray heating for A2597 because of insufficient X-ray intensity local to the filaments. Extremely slow shocks (<40 km s^{-1}) produce significantly higher $H_2/H\alpha$ ratios than do fast shocks, consistent with what we observe in A2597 and PKS 0745−191, but not very efficiently. In order to produce a constant observed luminosity, tens of thousands of solar masses of gas must be processed by the shocks in each source each year. We conclude that the radio sources are not injecting significant amounts of energy by strong shocks into the interstellar and intracluster medium—at best, the emission-line and molecular gas may be pushed around by the radio sources.

UV irradiation by very hot stars, implied by a star formation rate of only a few solar masses per year, is a possibility yet consistent with both the $H\alpha/H_2$ line ratios and UV continuum observations by *IUE*. One to 2 μm spectroscopy would definitively test this hypothesis because UV fluorescence produces significant amounts of $v = 2$ vibrational lines from excited molecular hydrogen. Also, if UV irradiation is the dominant mechanism, the far-infrared (~ 60 μm) luminosities should be not far below the *IRAS* upper limits inferred for A2597 and PKS 0745−191, $\sim 10^{44}\ h^{-2}$ ergs s^{-1}, easily detectable by *SIRTF* observations. Thermally heated molecular gas very efficiently radiates molecular hydrogen lines, so in the case of PKS 0745−191, the ambient X-ray gas might heat a small amount of molecular hydrogen. We cannot rule out conduction and turbulent mixing layers as plausible heat sources, although energetically, direct X-ray heating and turbulent mixing layers are unlikely. We conclude that UV irradiation is the most viable heat source for both PKS 0745−191 and A2597. If UV fluorescence is the dominant physical mechanism, $\sim 3 \times 10^9\ M_\odot$ of vibrationally excited H_2 exists in these cluster galaxies, while if the gas is thermally excited by X-rays or conduction, only $\sim 10{,}000\ M_\odot$ in each galaxy are implied.

These observations provide some insight into the physical processes that may be occurring in the cores of clusters with cooling flows. Vibrationally excited H_2 and dust lanes appear to exist in the same cooling flow clusters with optical emission-line nebulae. The H_2 emission is too bright to be produced directly by the cooling flow. The amount of H_2 implied to be present is at least a factor of 100 too small to account for a repository of molecular gas that has accumulated over a Hubble time of constant cooling, even if the emission is powered by the UV radiation from star formation. The star formation rate inferred from the $H\alpha$ and H_2 emission and an assumption of UV powering is also too small to account for cooling rates of greater than $100\ M_\odot$ yr^{-1}. However, these observations also show that the radio sources in these clusters do not impart a significant amount of shock energy to the emission-line gas and therefore cannot be a significant source of heating to counterbalance the cooling in the centers of cooling flows.

This work was supported by the NASA *HST* grant GO-7457. P. R. M. is supported by the NASA Astrophysical Theory Program under grant NAG 5-4061 and by NSF under grant AST 99-00871. This work is based partly on

observations made with the NASA/ESA *Hubble Space Telescope* obtained from the data archive at the Space Telescope Science Institute. Some of the data presented in this paper were obtained from the Multimission Archive at the Space Telescope Science Institute (MAST). Support for MAST for non-*HST* data is provided by the NASA Office of Space Science via grant NAG 5-7584 and by other grants and contracts. STScI is operated by the Association of Universities for Research in Astronomy, Inc., under NASA contract NAS 5-26555. This research has also made use of data obtained from the High Energy Archive Research Center (HEASARC), provided by NASA's Goddard Space Flight Center. We acknowledge extensive discussions and data reduction advice from David Zurek. We thank Eddie Bergeron, John Biretta, Mark Dickinson, Paul Goudfrooij, Roeland van der Marel, Cathy Imhoff, and Sylvia Baggett for very useful discussions. We are grateful to the anonymous referee for his or her comments. This research has made use of the NASA/IPAC Extragalactic Database (NED), which is operated by the Jet Propulsion Laboratory, California Institute of Technology, under contract with the National Aeronautics and Space Administration.

APPENDIX

GLOBULAR CLUSTERS AND DUST IN NGC 1275

The 1.6 μm image obtained in our program, co-added to a similar image taken for a parallel observing program, has yielded near-infrared photometry for the NGC 1275 star clusters first detected by Holtzman et al. (1992). We have extracted WFPC2 photometry for the same clusters in order to enable two-color studies with the *H*-band photometry. Our photometry procedure and results are reported here. We compare the colors obtained for these clusters with those predicted for a young stellar population with a single burst of star formation as a function of time since the burst, and we compare our results to those of optical *HST* photometry of the same star clusters (Carlson et al. 1998, hereafter C98).

A1. GLOBULAR CLUSTER PHOTOMETRY

The large number of centrally distributed globular clusters in NGC 1275 allows an estimate of individual globular cluster colors by comparing photometry with WFPC2 and NICMOS at *B*, *R*, and *H*. We use both our F160W data and archival data (Regan & Mulchaey 1998, Program 7330) to create a summed *H*-band image. The F450W and F702W archival images from Program 6228 (C98; Holtzman et al. 1996, 1992) were deep *B* and *R* images of the globular clusters in NGC 1275, with exposure times of 4900 and 4500 s, respectively.

In Figure 10, we present the 640 s exposure 1.6 μm image with the best-fit elliptical model subtracted and with globular cluster candidates marked. Compact clusters which were apparent in the NICMOS image and both the F450W and F702W images were chosen for comparison. Aperture photometry was performed using DAOPHOT, with the aperture size chosen to be the radius where the source PSF fades into the noise. This corresponds to 4 pixels for NICMOS (0.″30) and 3 pixels for the PC on WFPC2 (0.″14). Sky values were determined by estimating the mode of background in an annulus from 4 to 7 pixels for WFPC2 and from 5 to 8 pixels in NICMOS. We correct the fluxes to $r = 0.''5$ apertures by generating the PSF for each filter with Tiny TIM, matching the FWHM of the convolution of the model PSF with a two-dimensional Gaussian to the FWHM of the average globular cluster and estimating the appropriate flux correction.

The photometric zero points and color transformations were derived using SYNPHOT, allowing us to calculate the total magnitude and color of each globular cluster for Johnson *B* and *R* photometry and for *HST H* photometry. The zero point for the WFPC2 data (VEGAMAG) includes an aperture correction from $r = 0.''5$ to "infinite" aperture (0.10 mag). The NICMOS data zero points, on the other hand, are given for an $r = 0.''5$ aperture. To correct to "infinite" aperture, we multiplied the total count rate by 1.15, as recommended by the NICMOS photometry section on the NICMOS instrument Web site.[6] The zero points for each filter are listed in Table 8.

To derive the best Johnson color transformations, the spectral type of the objects must be known in advance. Brodie et al. (1998) compare the spectra of five globular clusters in NGC 1275 with standard stellar spectra covering a range of spectral types and luminosity classes. The best match to these spectra, early type A dwarfs and class III giants, was used as the model for transforming the *HST B* and *R* filters to the Johnson system. The resulting color corrections are negligible, 0.007 and 0.001 mag for each filter, respectively. The *HST* VEGAMAG system was used for the cluster *H*-band photometry. For reference, the color term required to correct the *HST* system to the KPNO *H* system is +0.034 mag. The corrections used for our photometric calibration are summarized in Table 8.

[6] http://www.stsci.edu/instruments/nicmos.

TABLE 8

PHOTOMETRY CORRECTIONS FOR STAR CLUSTERS IN NGC 1275

Magnitude System	Vega Zero Point (mag)	Aperture Correction (mag)	Color Correction (mag)
Johnson *B*	21.99 ± 0.02	−0.17	−0.01
Johnson *R*	22.43 ± 0.02	−0.21	−0.00
HST H	21.67 ± 0.05	−0.08	

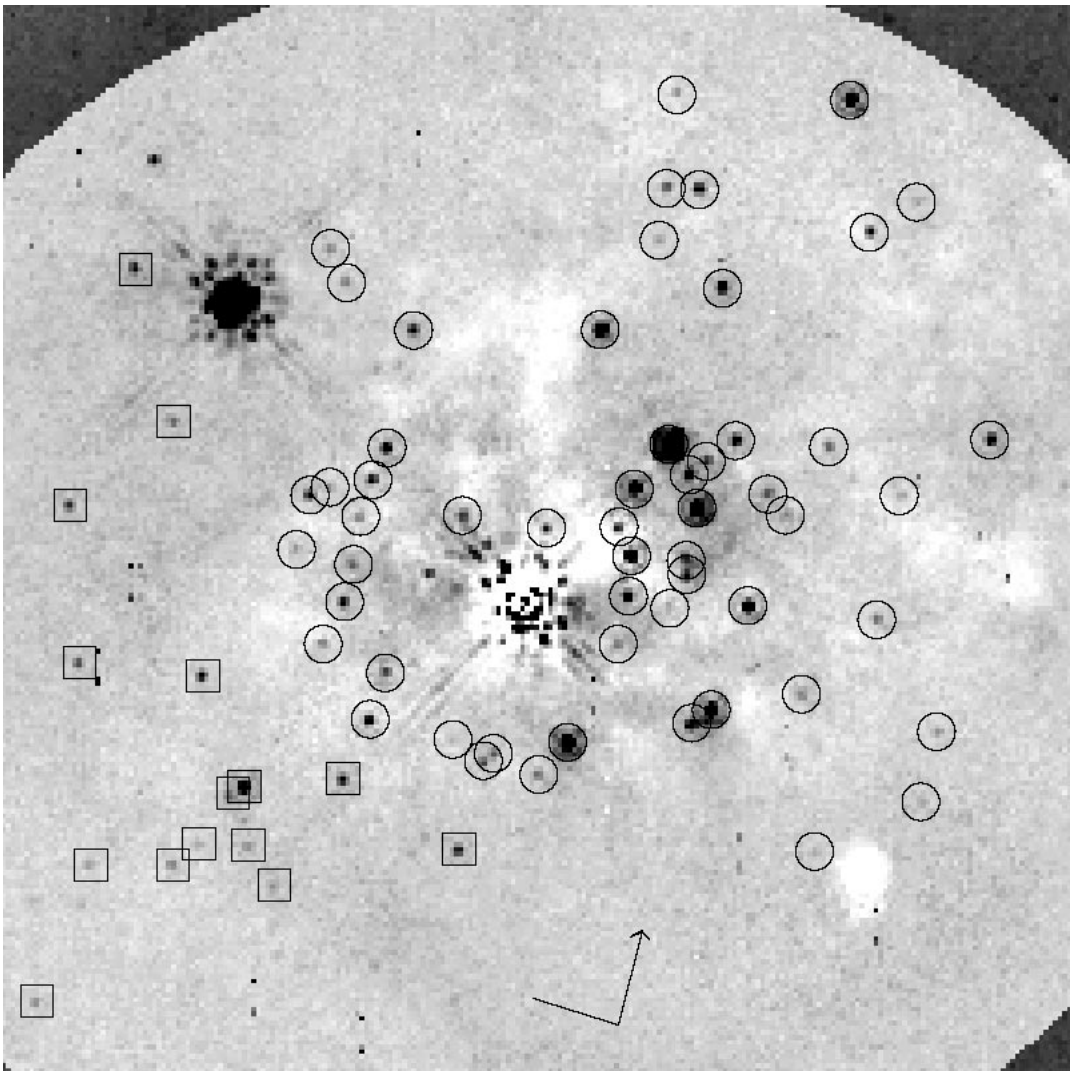

FIG. 10.—Star clusters in NGC 1275. An ellipsoidal model has been subtracted from the 1.6 μm *HST* data. White regions outline dust lanes; dark spots are star clusters. Nucleus and a foreground star appear as prominent point sources with diffraction spikes and Airy rings in center and upper left of image. Circular white absorption feature in lower right-hand corner is the coronograph. Edges of ellipsoidal model are visible in corners of image. Boxed clusters lie in same lines of site as the regions which appear to be free of dust lanes. Circled objects indicate other clusters which most likely lie in same lines of site as the dust lanes. North is marked with arrow.

C98 presented an analysis of the compact star clusters in NGC 1275 using deep WFPC2 images at B and R bands, the same data we retrieved from the archive. They present $B-R$ color versus B magnitude plots for all clusters in the PC and the WFs and separately for clusters in the relatively dust-free southwest portion of the PC. This analysis revealed a bimodal color distribution, with a blue population having $(B-R)_0 = 0.4$ and a red population with $(B-R)_0 = 1.3$. The red objects are members of an old globular cluster system, while the blue clusters are a much younger population. The inferred age of the blue star clusters was derived using Bruzual-Charlot models (Bruzual & Charlot 1993) and the measured $B-R$ colors, indicating a range from 10^7 to 10^9 yr.

Because the extinction is so much less at H band than at B or R, the $B-H$ colors could produce an age estimate less dependent on assumptions about dust. In Figure 11 (*first column*) we present the photometry of all objects detected at 1.6 μm by plotting color against apparent magnitude, assuming Galactic extinction to be 0.71, 0.40, and 0.10 magnitudes at B, R, and H, respectively. Following the methods of C98, we tested whether the observed scatter in color was a result of internal extinction. Therefore, for this analysis, we chose clusters from the isophotal residual image which were clearly separate from the dusty regions. These clusters are indicated in Figure 10 and are plotted in Figure 11 (*second column*).

We find that the majority of our selected objects belong to the blue population described by C98, although we do detect a few of the red clusters, which are intrinsically fainter. The dominance of blue population objects is due to the shallower depth of the H-band data, thus limiting our sample to the brighter (and therefore bluer) clusters in the field. By limiting the photometry to dust-free regions of the image, the scatter in the observed $(B-R)$ colors decreases from 0.23 to 0.08 mag. This scatter is consistent with the photometric errors, supporting the idea that varying amounts of dust extinction, rather than differences in age, are responsible for the dispersion in the measured colors of each population.

The blue clusters have a typical $(B-R)$ color of 0.5 mag and $(B-H)$ color of 1.7 mag. Figure 11 (*third column*) shows the Bruzual-Charlot color evolution (Bruzual & Charlot 1993) of a single-burst population, assuming a Salpeter initial mass

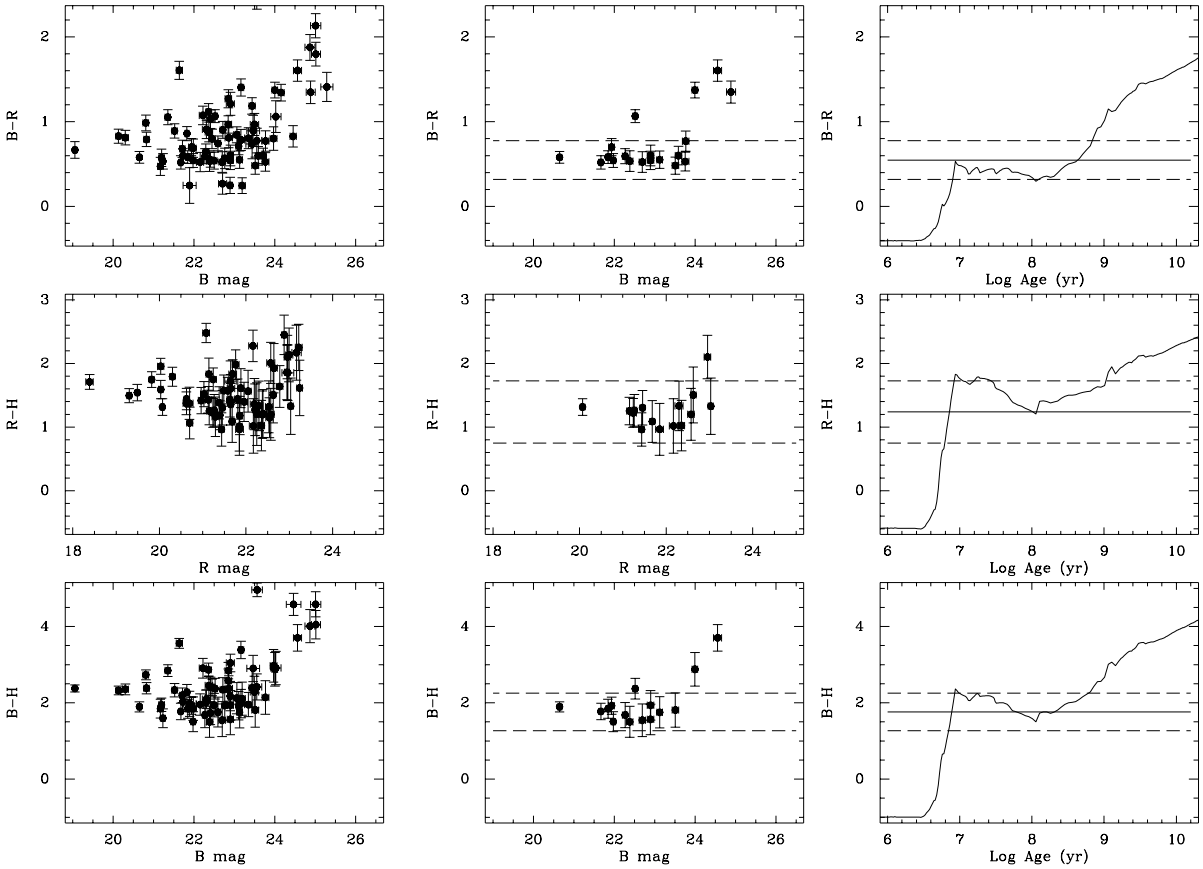

FIG. 11.—Cluster photometry and age determinations. Points are the photometry data with 1 σ error bars. Dashed lines in plots in second and third columns delineate 3 σ dispersion of color photometry of the dust-free sample of blue clusters. (*First column*) Magnitude-color plots for all clusters in sample. (*Second column*) Magnitude-color plots for the clusters in the nondusty regions. (*Third column*) 3 σ color limits (*dashed lines*) and average colors (*solid straight line*) overlaid on single-burst Bruzual-Charlot model (*solid line*) of color vs. age. This plot shows that the cluster colors are consistent with ages of 10^7–10^9 yr.

function (IMF) from 0.1 to 125 $M_\odot$ and a total mass of 1 $M_\odot$. Dashed lines indicate the 3 σ dispersion of the blue cluster photometry, allowing us to infer ages from 10^7 to 10^9 yr. The effect of eliminating internal extinction by performing the photometry in the infrared has little effect in constraining the age of these clusters, since the $B-R$ and $B-H$ colors are insensitive within this age range.

Therefore, we confirm the age estimates of C98 by using optical near-infrared colors of the star clusters. We have also demonstrated, by selecting a subsample of stellar clusters from the dust-free regions of the infrared image, that the scatter in $B-R$ color is consistent with a scatter in the intrinsic dust absorption and not in cluster properties such as age.

REFERENCES

Allen, S. W. 2000, MNRAS, 315, 269
Baum, S. A., & O'Dea, C. P. 1991, MNRAS, 250, 737
Begelman, M. C., & Fabian, A. C. 1990, MNRAS, 244, P26
Black, J. H., & van Dishoeck, E. F. 1987, ApJ, 322, 412 (BvD87)
Braine, J., Wyrowski, F., Radford, S. J. E., Henkel, C., & Lesch, H. 1995, A&A, 293, 315
Bridges, T. J., & Irwin, J. A. 1998, MNRAS, 300, 967
Brocklehurst, M. 1971, MNRAS, 153, 471
Brodie, J. P., et al. 1998, AJ, 116, 691
Bruzual, A. G., & Charlot, S. 1993, ApJ, 405, 538
Burbidge, E. M., & Burbidge, G. R. 1965, ApJ, 142, 1351
Cardelli, J. A., Clayton, G. C., & Mathis, J. S. 1989, ApJ, 345, 245
Cardiel, N., Gorgas, J., & Aragon-Salamanca, A. 1995, MNRAS, 277, 502
———. 1998, MNRAS, 298, 977
Carlson, M. N., et al. 1998, AJ, 115, 1778
Crawford, C. S., Fabian, A. C., Johnstone, R. M., & Arnaud, K. A. 1989, MNRAS, 236, 277
Donahue, M., & Stocke, J. T. 1994, ApJ, 422, 459
Donahue, M., Stocke, J. T., & Gioia, I. M. 1992, ApJ, 385, 49
Donahue, M., & Voit, G. M. 1993, ApJ, 414, L17
Edge, A. C., & Stewart, G. C. 1991, MNRAS, 252, 414
Elston, R., & Maloney, P. 1992, BAAS, 181, 118.11
———. 1994, in Infrared Astronomy with Arrays: The Next Generation, ed. I. S. McLean (Kluwer: Dordrecht), 169
Fabian, A. C. 1994, ARA&A, 32, 277
Fabian, A. C., et al. 1985, MNRAS, 216, 923
Falcke, H., Rieke, M. J., Rieke, G. H., Simpson, C., & Wilson, A. S. 1998, ApJ, 494, L155
Ferland, G. J., Fabian, A. C., & Johnstone, R. M. 1994, MNRAS, 266, 399
Fischer, J., Smith, H. A., Geballe, T. R., Simon, M., & Storey, J. W. V. 1987, ApJ, 320, 667
Gehrz, R. D., Sramek, R. A., & Weedman, D. W. 1983, ApJ, 267, 551
Goudfrooij, P., & Trinchieri, G. 1998, A&A, 330, 123
Hansen, L., Jorgensen, H. E., & Norgarrd-Nielsen, H. U. 1995, A&A, 297, 13
Heckman, T. M., Baum, S. A., Van Breugel, W. J. M., & McCarthy, P. 1989, ApJ, 338, 48
Hill, G. J., Goodrich, R. W., & Depoy, D. L. 1996, ApJ, 462, 163
Hollenbach, D., & McKee, C. F. 1989, ApJ, 342, 306
Holtzman, J. A., et al. 1992, AJ, 103, 691
———. 1995, PASP, 107, 156
———. 1996, AJ, 112, 416
Hu, E. M. 1992, ApJ, 391, 608
Hu, E. M., et al. 1983, ApJ, 275, L27
Hunstead, R. W., Murdoch, H. S., & Shobbrook, R. R. 1978, MNRAS, 185, 149
Inoue, M. Y., Kameno, S., Kawabe, R., Inoue, M., Hasegawa, T., & Tanaka, M. 1996, AJ, 111, 1852
Jaffe, W., & Bremer, M. N. 1997, MNRAS, 284, L1

Johnstone, R. M., Fabian, A. C., & Nulsen, P. E. J. 1987, MNRAS, 224, 75
Kawara, K., & Taniguchi, Y. 1993, ApJ, 410, L19
Kenney, J. D. P., Rubin, V. C., Planesas, P., & Young, J. S. 1995, ApJ, 438, 135
Koekemoer, A. M., O'Dea, C. P., Sarazin, C. L., McNamara, B. R., Donahue, M., Voit, G. M., Baum, S. A., & Gallimore, J. F. 1999, ApJ, 525, 621
Krabbe, A., Sams, B. J., III, Genzel, R., Thatte, N., & Prada, F. 2000, A&A, 354, 439
Lazareff, B., Castets, A., Kim, D.-W., & Jura, M. 1989, ApJ, 336, L13
Lepp, S., & McCray, R. 1983, ApJ, 269, 560
Maloney, P. R., Hollenbach, D. J., & Tielens, A. G. G. M. 1996, ApJ, 466, 561
McNamara, B. R. 1997, in ASP Conf. Ser. 115, Galactic Cluster Cooling Flows, ed. N. Soker (San Francisco: ASP), 109
McNamara, B. R., & Jaffe, W. 1994, A&A, 281, 673
McNamara, B. R., Jannuzi, B. T., Sarazin, C. L., Elston, R., & Wise, M. 1999, ApJ, 518, 167
McNamara, B. R., & O'Connell, R. W. 1992, ApJ, 393, 579
———. 1993, AJ, 105, 417
Moshir, M., et al. 1990, *IRAS* Faint Source Catalog, Ver. 2.0 (Greenbelt: NASA/GSFC)
Mushotzky, R. F., Holt, S. S., Smith, B. W., Boldt, E. A., & Serlemitsos, P. J. 1981, ApJ, 244, L47
O'Dea, C. P., Baum, S. A., & Gallimore, J. F. 1994a, ApJ, 436, 669
O'Dea, C. P., Baum, S. A., Maloney, P. R., Tacconi, L. J., & Sparks, W. B. 1994b, ApJ, 422, 467
Osterbrock, D. E. 1989, Astrophysics of Gaseous Nebulae and Active Galactic Nuclei (Mill Valley: University Science Books)
Pedlar, A., Ghatuaure, H. S., Davies, R. D., Harrison, B. A., Perley, R., Crane, P. C., & Unger, S. W. 1990, MNRAS, 246, 477
Peres, C. B., Fabian, A. C., Edge, A. C., Allen, S. W., Johnstone, R. M., & White, D. A. 1998, MNRAS, 298, 416
Pierre, M., & Starck, J.-L. 1998, A&A, 330, 801
Pinkney, J., et al. 1996, ApJ, 468, L13
Quillen, A., et al. 1999, ApJ, 527, 696
Regan, M. W., & Mulchaey, J. S. 1998, BAAS, 193, 6.05
Sarazin, C. L., Burns, J. O., Roettiger, K., & McNamara, B. R. 1995, ApJ, 447, 559
Seaton, M. J. 1979, MNRAS, 187, P73
Seyfert, C. K. 1943, ApJ, 97, 28
Shull, J. M., Roberts, D., Giroux, M. L., Penton, S. V., & Fardal, M. A. 1999, AJ, 118, 1450
Singh, K. P., Prabhu, T. P., Kembhavi, A. K., & Bhat, P. N. 1994, ApJ, 424, 638
Sparks, W. B., Ford, H., & Kinney, A. 1993, ApJ, 413, 531
Sparks, W. B., Macchetto, F., & Golombek, D. 1989, ApJ, 345, 153
Strauss, M. A., Huchra, J. P., Davis, M., Yahil, A., Fisher, K. B., & Tonry, J. 1992, ApJS, 83, 29
Struble, M. F., & Rood, H. J. 1987, ApJS, 63, 543
Thompson, R. L., Rieke, M., Schneider, G., Hines, D. C., & Corbin, M. 1998, ApJ, 492, L95
Voit, G. M., & Donahue, M. 1990, ApJ, 360, L15
———. 1995, ApJ, 452, 164
———.1997, ApJ, 486, 242
Walterbos, R. A. M., & Kennicutt, R. C., Jr. 1988, A&A, 198, 61
Wise, M., O'Connell, R., Bregman, J., & Roberts, M. S. 1993, ApJ, 405, 94
Yan, L., & Cohen, J. G. 1995, ApJ, 454, 44